Paul Maierhofer BSc

Femtosecond Photodissociation Dynamics in Molecules studied by Time-Resolved Photoelectron-Photoion-Coincidence Spectroscopy

MASTER'S THESIS

to achieve the university degree of

Diplom-Ingenieur

Master's degree programme: Technical Physics

submitted to

Graz University of Technology

Supervisor

Ass.Prof. Dipl.-Ing. Dr.techn. Markus Koch

Institute of Experimental Physics

Graz, July 2016

AFFIDAVIT

I declare that I have authored this thesis independently, that I have not used other than the declared sources/resources, and that I have explicitly indicated all material which has been quoted either literally or by content from the sources used. The text document uploaded to TUGRAZonline is identical to the present master‘s thesis.

Date

Signature

Abstract

Within this work a pump-probe laser setup for time-resolved femtosecond spectroscopy was designed, constructed, characterised and used for the investigation of relaxation dynamics in acetone. The beam of a commercial femtosecond laser (sub 25 fs pulse length, 800 nm central wavelength) was split into a pump and a probe path where frequency doubling and collinear frequency mixing led to 400 nm and 266 nm pulses respectively. By collinear superposition of the pulses, an overlap in the ionization region of a time-of-flight spectrometer is achieved. The investigated species which is in gas phase is excited by the pump and ionized by the probe pulse. With a pulsed electric field both ions and electrons from the same ionization event can be detected which leads to photoelectron-photoion-coincidence-spectroscopy (PEPICO). This highly selective experimental technique provides essential information on photochemical processes and molecular dynamics.
The setup was used to investigate molecular dynamics initiated by two photon excitation with 4.6 eV photon energy in acetone where multiple energy states lie resonant with the pump photon energy. These states undergo ultrafast relaxations via internal conversion which leads to a pump-probe time-delay dependent signal. Due to complex relaxation mechanisms several ionization channels are possible. PEPICO allows a channel resolved measurement of the electron spectra which provides essential information for the correct interpretation of the dynamics. We were able to identify three distinct ionization channels with different transition and ionization states. The time evolution of these channels and the fragmentation behaviour was determined.

Kurzfassung

Es wurde ein Pump-Probe Laser Setup für zeitaufgelöste Spektroskopie entworfen, aufgebaut und charakterisiert, sowie letztlich zur Untersuchung von photoinduzierten Moleküldynamiken in Aceton verwendet. Dazu wurden Pulse eines kommerziellen Femtosekunden-Lasers (unter 25 fs Pulslänge, 800 nm zentrale Wellenlänge) in einen Pump und einen Probe Zweig geteilt. Durch Frequenzverdopplung und kollineare Frequenzmischung wurden 400 nm bzw. 266 nm Pulse erzeugt. Durch kollineares Übereinanderlegen der Pulse kann ein Überlappen am Ort der Ionisation in einem Flugzeit-Spektrometer sichergestellt werden. Dort befinden sich die zu untersuchenden Moleküle in Gasphase, werden vom Pump angeregt und weiters vom Probe ionisiert. Durch die Verwendung eines gepulsten Abzugsfeldes lassen sich sowohl Elektronen als auch Ionen des selben Ionisationsevents detektieren - dies führt zur Photoelektron-Photoion-Koinzidenz-Spektroskopie (PEPICO). Diese sehr trennscharfe Methode liefert entscheidende Informationen über photochemische Prozesse und Moleküldynamiken.
Das Setup wurde zur Untersuchung von Moleküldynamiken in Aceton verwendet, da hierbei resonante Zustände mit der Pump Photonenenergie von 4.6 eV vorliegen. Diese Zustände zeigen schnelle Relaxationen durch Internal Conversion, was eine Abhängigkeit der Signale vom Zeitversatz zwischen Pump und Probe zur Folge hat. Die komplexen Relaxationsmechanismen führen zu verschiedenen Ionisationskanälen. PEPICO erlaubt eine Ionisationskanal-aufgelöste Messung der Elektronenspektra, dies ermöglichte die Identifikation dreier Kanäle mit verschiedenen Zwischenzuständen. Die Zeitentwicklung dieser Kanäle und ihr Fragmentationsverhalten wurde bestimmt.

Contents

CHAPTER 1

Introduction

Photoinduced dynamics in molecules is not only an interesting and intensely studied field but also governs parts of our daily life. For example photosynthesis, the formation of vitamin D with sunlight, or vision are just a few examples where the interaction of photons with matter plays an important role in chemistry. A deep understanding of photochemical processes is therefore crucial for our understanding of nature and may also play a key role for future technologies such as photo-polymerization e.g used for 3D printers, the conversion and storage of solar energy, or in medical applications both for diagnostics and therapy. [1]

The aim of the Koch group is to get a better understanding of photoinduced dynamics in general. The state of the art experimental setup designed for ultrafast femtosecond time-resolved pump-probe photoelectron-photoion coincidence (PEPICO) spectroscopy is able to provide unequivocal information on dynamics where charged particles are formed. The investigated species is hereby in gas phase in order to do experiments on isolated molecules. The following sections will provide an overview of principle photochemical reactions and applied experimental methods such as PEPICO.

1.1 Photochemistry

1.1.1 Overview

When one or more photons are absorbed by an atom or a molecule, the energy brought into the system will induce dynamics as the energy is distributed among other degrees of freedom. In principle the geometry, chemical structure, eletronic, vibrational and rotational states of the species can be affected - multiple pathways are possible. See fig.1.1. The following section is -if not indicated - an excerpt from ref. [1].

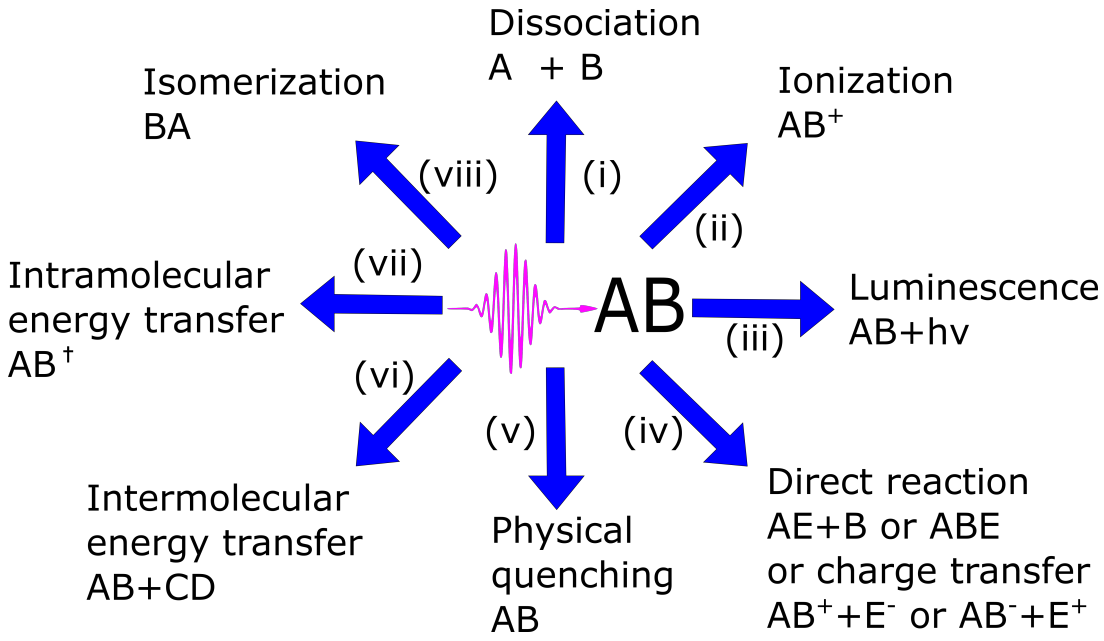

Figure 1.1: Possible pathways of relaxation after a photon is absorbed by a molecule AB consisting of groups A and B.

Dissociation (i)

Dissociation upon excitation will occur both if the excitation leads to an unbound state of A and B or if the energy brought into the system is higher than the dissociation energy of the molecule. The fragments will take up the excess energy in form of translational energy. Dissociation can take place in the neutral molecule but can also be a result of ionization when the ionic state that is reached is not a bound state.
Also predissociation plays an important role especially for complex molecules. Via radiationless relaxation (see subsection (vii)) the molecule ends up in a repulsive state which crosses a bound state.

Ionization (ii)

For the case of PEPICO experiments the most important impact of photons on molecules is ionization. When an electron is promoted to a state above the ionization potential (I_p) by n photons the electron gains excess energy relative to the I_p and the ponderomotive potential U_P caused by the laser field in form of kinetic energy E_kin.

$$E_\mathrm{kin} = nh\nu - (I_\mathrm{P} + U_\mathrm{P}) \tag{1.1}$$

as provided by [2]. Also autoionization can occur in molecules. Herby multiple electrons are excited in states below $\mathrm{I_P}$. Upon relaxation the excess energy is transferred to one electron which then leads to ionization [2]. E.g. the excitation of the HOMO-1 electron can lead to autoionization.

Luminescence (iii)

Luminescence is the relaxation with the emission of radiation. Basically two cases can be distinguished. Phosphorescence is a radiative transition between states of different multiplicities whereas fluorescence is a radiative transition between states that have the same multiplicity. See fig.1.2.

In principle direct excitation to a state of different multiplicity than the ground state is forbidden for small systems and has a small probability for larger molecules. Therefore the main pathway to phosphorescence is excitation without change of multiplicity followed by a relaxation to another state of different multiplicity via intersystem crossing (ISC). (see subsection (vii)) The example in fig.1.2 shows the excitation from a singlet state ^{1}A to another singlet state ^{1}A*, this state undergoes intersystem crossing to a triplet state ^{3}A which has lower energy than ^{1}A which happens to be a typical case. The direct relaxation from ^{1}A* to ^{1}A is called fluorescence while the transition from ^{3}A to ^{1}A depicts phosphorescence.

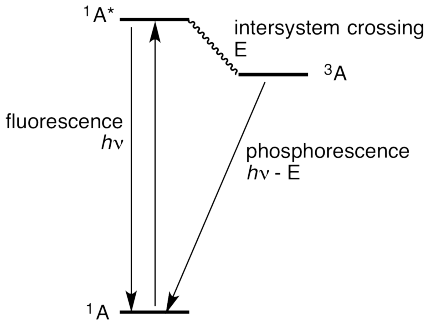

Figure 1.2: Principle of fluorescence and phosphorescence. [1]

[1] from `https://en.wikipedia.org/wiki/Jablonski_diagram`

Direct Reaction and Charge transfer (iv)

Excited molecules of course react in a different way than in the ground state which leads to reactions that are not accessible without the presence of photons. By absorption, internal conversion and intersystem crossing (see subsection (vii)) reactive states can be reached. Processes where an electron is transferred from one atom to another or from an ion to solvents are examples for charge transfer. For gas-phase experiments such as the experiments done within this thesis, these processes are not possible as the particle density is low.

Physical Quenching (v)

Quenching is a special case of intermolecular energy transfer which becomes important especially in the liquid phase where collisions take place very frequently and the excitation in the acceptor molecule can be neglected. The energy gets redistributed in vibrational, rotational, and translational energy in the acceptor species.

Intermolecular energy transfer (vi)

Energy transfer between different molecules is possible via different mechanisms. There are no strict selective rules as there is always the possibility to convert electronic or vibrational energy to kinetic energy. The simplest transfer mechanism is the collision which is a short range interaction. Coulombic interaction is long-range and governed by dipole interaction which overshadows higher order multipole interactions. For gas-phase experiments these processes are not possible.

Intramolecular energy transfer (vii)

Intramolecular energy transfer is one of the most important processes. Herby the excited electronic state determines the dynamics. The two distinguished processes are intersystem crossing (ISC), where states with different multiplicities come close in energy and therefore a transition is possible, and internal conversion (IC) where the spin and therefore the multiplicity of the involved states is conserved. In both processes electronic energy is converted to other degrees of freedom such as the nuclear geometry of the molecule and vibrational and rotational energy. ISC is herby an important mechnism to populate states which have a small probability for direct excitation. See fig.1.2.

A common term in this context is IVR which is short for intramolecular vibrational redistribution where energy is stored in vibrational energy which is distributed in the molecule. These processes can lead to fragmentation as bonds break by an overload of vibrational energy. These processes are of great interest in gas-phase experiments.

Isomerization (viii)

Excitation of molecules can remove constrains for the molecule to be in a fixed geometry. This way excitation of cis- and trans- isomers leads to an equivalent excited state. By relaxation isomers are again formed, both cis-trans and trans-cis transitions can be introduced.

All these processes take place on different time scales. While ionization takes only a few attoseconds, luminescence can last up to several microseconds. The most important reactions for PEPICO experiments are the ionization which is necessary to obtain signals at all, as well as dissociation and intramolecular energy transfer which are processes that are accessible for investigations with femtosecond spectroscopy.
Additionally so called Norrish-type reactions are important in ketones such as actone, which was studied within this thesis.

1.1.2 Norrish-type reactions I and II

Especially for species containing the C=O carbonyl group, such as ketones and aldehydes there are two important dissociative primary photochemical processes, namely Norrish-type I and Norrish-type II.

In Norrish-type I (see fig.1.3) the carbonyl group absorbs a photon (around 280 nm for ketones). This state typically undergoes ISC to a triplet state which then fragments into two radicals. Subsequently the radicals can recombine or undergo further chemical processes.

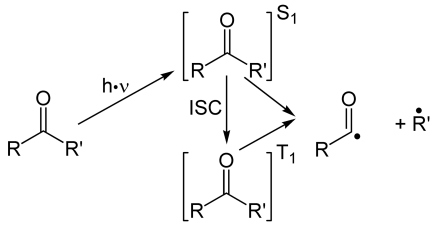

Figure 1.3: Principle of Norrish-type I reaction. [2]

[2] https://de.wikipedia.org/wiki/Norrish-Reaktion

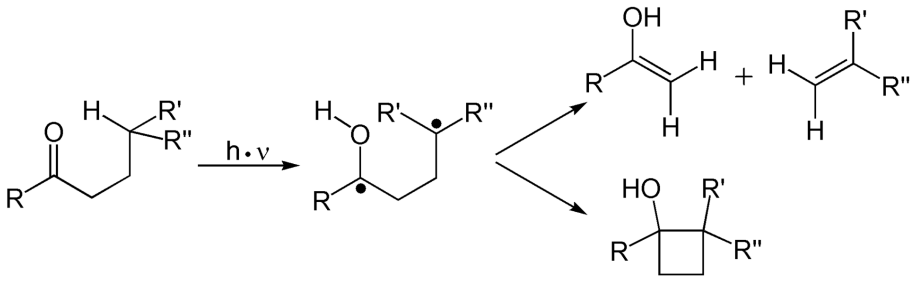

Figure 1.4: Principle of Norrish-type 2 reaction. [2]

Fig.1.4 schematically depicts a Norrish-type II process. Herby a hydrogen atom is transferred to the carbonyl group which leads to a bi-radical. This biradical can further fragment to an enol and an alkene or rearrange to a substituted cyclo-butane.

1.2 Experimental Approaches

Experimental approaches on the fragmentation and dissociation dynamics of molecules in the context of our setup include the acquisition of ultrafast time-resolved photoelectron spectra [3–8], photoion mass spectra [9, 10] as well as photoelectron-photoion-coincidence spectroscopy [11]. In all these cases the studied species is excited by a pump laser pulse and later on ionized by a probe laser pulse - the pulse durations are typically on a femtosecond timescale in order to resolve dynamics. In order to obtain spectra the fragments and/or electrons are detected by a time-of-flight spectrometer. The transient spectra give insight in the dynamics in the species as the signal is dependent on the the time delay between pump and probe pulse which equals the time the excited species has to undergo relaxation.

PhotoElectron-PhotoIon-COincidence-spectroscopy PEPICO

By using a pulsed repeller voltage (details see ref. [12]) both electrons and ions can be detected from the same ionization events which leads to PEPICO, a technique which is able to provide fragment resolved electron-spectra. Both time-resolved photoelectron and photoion spectra are able to provide deep insight on molecular dynamics but lack of the ability to distinguish ionization channels and whether fragmentation takes place in the neutral molecule or if ionization leads to fragmentation which can lead to misinterpretation, see chapter 3.3.1. Only PEPICO is able to provide channel-resolved photoelectron

spectra which provides crucial information for the correct interpretation of time-resolved pump-probe experiments.
Other experimental approaches include for example TPEPICO which is short for Threshold-PEPICO where electrons with zero kinetic energy are detected which indicate the presence of auto-ionisation states. [13] Cold Target Recoil Ion Momentum Spectroscopy - COLTRIMS is a technique where the geometry of a molecule can be reconstructed by velocity mapping of the fragments. [14, 15]

CHAPTER 2

Experimental Setup

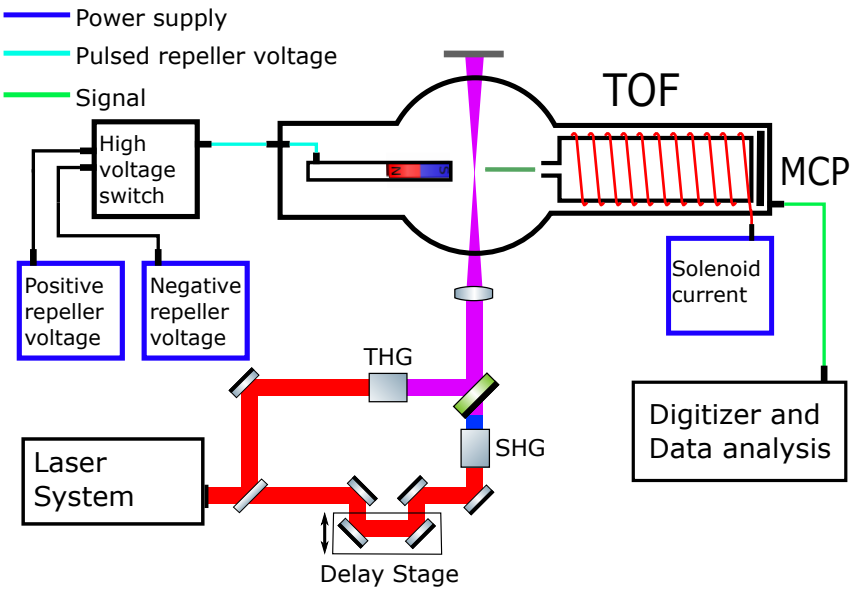

Figure 2.1: Experimental setup for ultrafast femtosecond time-resolved 266 nm pump 400 nm probe photoion-photoelectron coincidence spectroscopy. [12]

The present experimental setup sketched in fig.2.1 is used for ultrafast femotsecond time-resolved 266 nm pump 400 nm probe photoelectron-photoion spectroscopy. This setup is used for the investigation of photoinduced dynamics in atoms or molecules on a femtosecond timescale. A pump pulse excites the population of the investigated species which is in gaseous phase in the spectrometer. A probe pulse with a variable time delay to the pump pulse ionizes the excited molecules. The generated ions and electrons are pushed by suitable voltages and a magnetic field at the repeller and in the flight tube of a time

of flight (TOF) spectrometer, provided by a solenoid, to the micro-channel-plate (MCP) where the hits are converted to an electric signal. The signal is digitized and further analysed. From the times of flights the masses of the detected ion hits and the kinetic energies of the electrons are calculated which reveal dynamics of the species. With a pulsed voltage at the repeller both ions and electrons of the same ionization event can be detected which leads to PhotoElectron-PhotoIon-Coincidence spectroscopy (PEPICO).
In the following chapters a detailed explanation of the key elements of the optical setup will be given. The spectrometer, data acquisition and data analysis tools are explained in detail within the master's thesis of Markus Bainschab. [12]

2.1 Optical Setup

Before a more detailed explanation of the key elements of the setup will be given in the following sections, an overview will be provided.

2.1.1 Overview

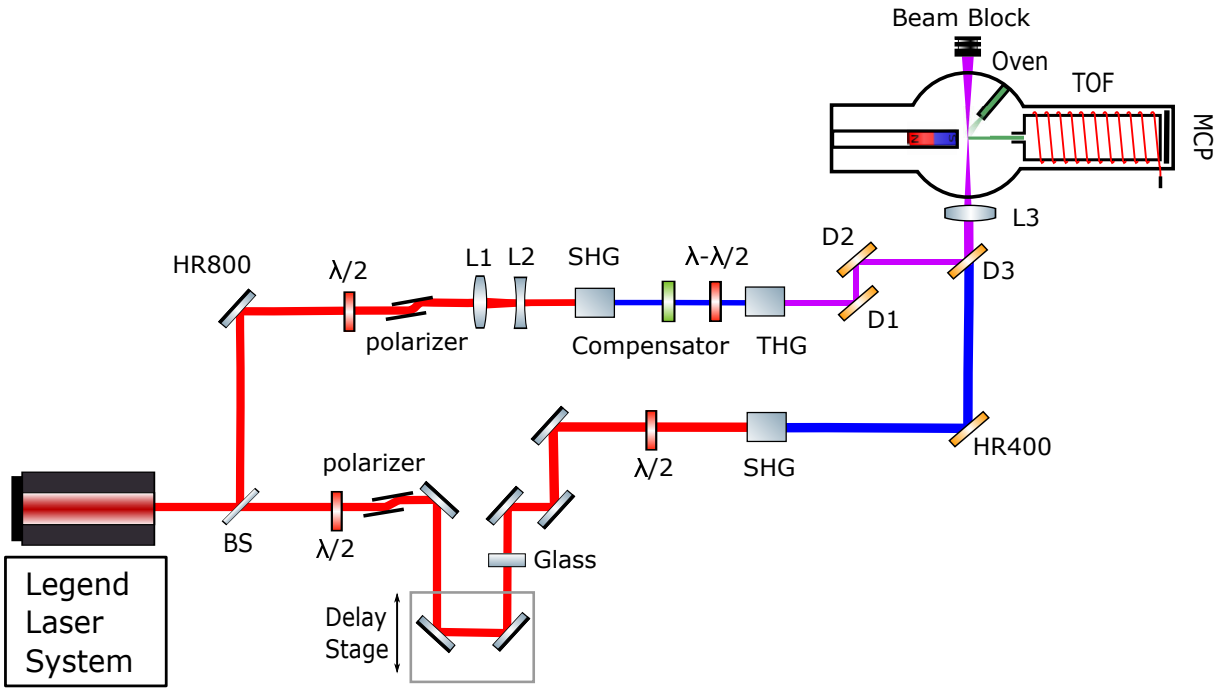

Figure 2.2: Optical Setup for ultrafast femtosecond time-resolved 266 nm pump 400 nm probe wavelength photoion-photoelectron coincidence spectroscopy. The elements are described in the text.

Figure 2.2 shows an overview of the optical setup of the experiment.
The laser system itself is a commercial Ti:Sapphire laser from Coherent Inc., namely a Vitara oscillator and a Legend Elite Duo amplifier. The pulse length at the output is approximately 25 fs with a repetition rate of 3 kHz and a central wavelength of 800 nm, the output power is approximately 13.3 W. Right after the output comes a beamsplitter (BS, Newport, part number: 20RQ00UB.2) which reflects 30% of the power for vertical polarization. The transmitted part is frequency doubled and further used as the probe pulse of the experiment. By a have wave plate ($\lambda/2$) and two thin film polarizers which are aligned in Brewster's angle, the power of the transmitted beam can be manipulated. A delay stage is used in order to change the time delay of the pump and the probe pulse. After the delay stage the polarization of the pulse is changed to horizontal in order to have a vertical polarized pulse in the spectrometer. The pulse is frequency doubled by a BBO crystal by second harmonic generation (SHG). As there is a remaining part of the beam with 800 nm wavelength, a dicroic mirror has to be used with a high reflectance at 400 nm and a high transmission at 800 nm (HR400) in order to get rid of the 800 nm part. The reflected part of the beam at BS also passes a $\lambda/2$ plate and thin film polarizers for power control. Afterwards a telescope is used to narrow the diameter of the beam in order to match the size of the following crystals to increase the conversion efficiency. A SHG BBO crystal will double the frequency, a group delay compensator (Compensator) will match the 400 nm and the remaining 800 nm part of the pulse in time. The polarization of the 800 nm is rotated by 90 degrees in order to have a vertical polarization of the 266 nm pulse after the third harmonic generation (THG) in a BBO crystal by sum frequency mixing. After the THG the pulse consists not only of 266 nm but also of 800 nm and 400 nm fractions. These remaining parts are blocked by using dicroic mirrors which are highly reflecting at 266 nm (D1, D2 and D3, see ref.2.1.4). Three of these mirrors are used in order to get a mostly pure 266 nm pulse. At D3 pump and probe beams are united again as the 266 nm pulse of the pump is reflected while the 400 nm probe beam is transmitted. A focusing lens (L3, focal length 500 mm) is used in order to focus the beams in the spectrometer where atoms or molecules are ionized and consequently electron energies and ion masses can be measured with the help of an time of flight spectrometer(TOF) and a multi channel plate (MCP). The beam is blocked after it has passed the spectrometer.

2.1.2 Second Harmonic Generation SHG

Table 2.1: Parts for SHG setup

label	company	part no.
SHG BBO Crystal 100 μm	Newlight Photonics	BTC5010-SHG800(I)-AR
SHG BBO Crystal 500 μm	Newlight Photonics	BTC5050-SHG800(I)-AR
Halfwaveplate	Thorlabs	AHWP10M-980
Dicroic Mirror HR400HT800	Lasercomponents	HR400HT800/45/BBAR-D PW1012UV

In tab.2.1 the main parts for the SHG setup are listed.
A Type 1 BBO crystal was used, which converts two 800 nm photons of the same polarization to one 400 nm photon with a polarization orthogonal to the incoming ones. As the desired polarization in the spectrometer is vertical, a halfwaveplate is used to change the polarization of the 800 nm photons to horizontal. Therefore, a Nicol prism is used to check the polarization. After the halfwaveplate follows the SHG BBO crystal. Either a 100 μm or 500 μm thick crystal can be used. The thicker one has the advantage of a better conversion efficiency and a broader phasematching leading to a lower 800 nm part, a broader spectrum of the frequency doubled pulse but also the disadvantage of an increased chirp.
The disadvantage of the collinear setup is that after SHG the fundamental part comes collinear with the first harmonic. In order to separate fundamental from first harmonic, a suitable dicroic mirror has to be used which has a high reflectivity at 400 nm and a high transmission at 800 nm. (HR400, see sec.2.1.4) By monitoring the reflected power the alignment of the crystal can be adjusted for maximum conversion efficiency. In the following fig.2.3 the spectrum after the HR400 mirror is shown. The central wave length at the maximum of the conversion efficiency is 405 nm (see section 2.1.11 for more details). Note that there is still a relatively big part 800 nm left which can cause misleading results, depending on the investigated species. When the setup is changed to another wavelength or main optical components such as crystals or dicroic mirrors are changed, the spectrum of the beam has to be checked with the spectrometer or the prism.

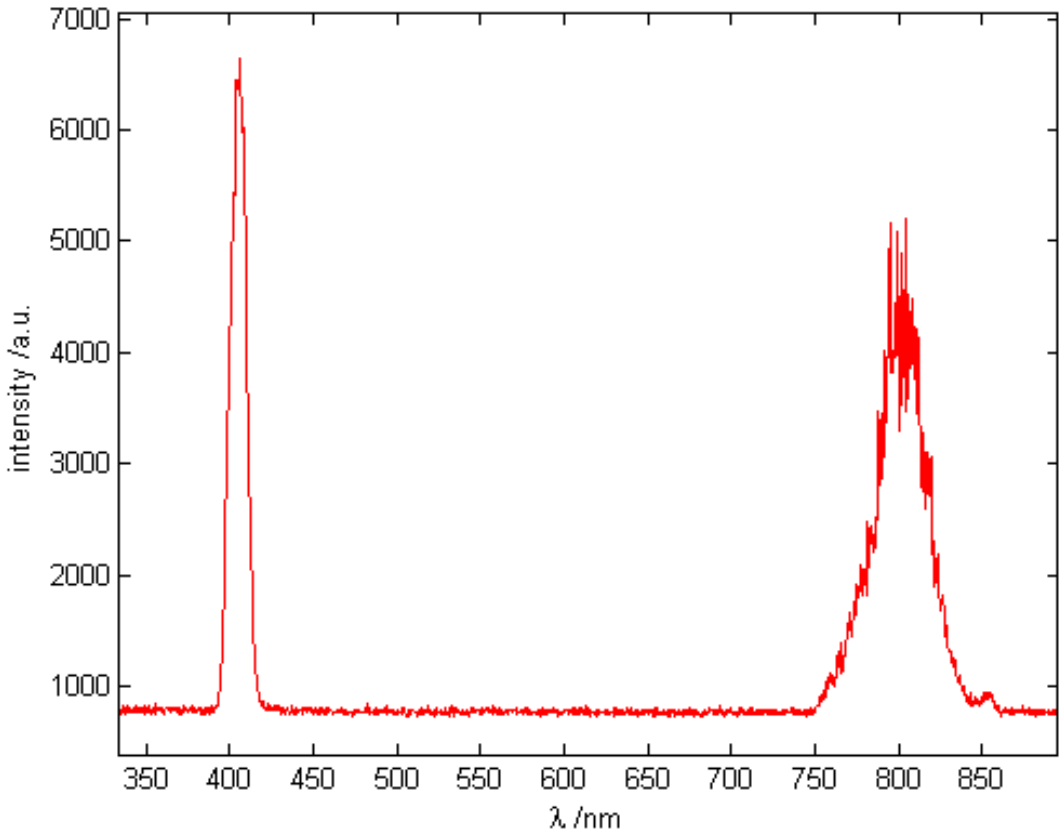

Figure 2.3: Spectrum of the pulses after SHG using the 100 μm thick crystal and the dicroic mirror HR400.

The spectrum of the probe pulse can be shifted from 397 nm to 405 nm central wavelength whereas the conversion efficiency is best for 405 nm. Note that small differences in the central wavelength of a few nm can have a significant impact on the experimental results. [12]

2.1.3 Third Harmonic Generation

Table 2.2: Parts for THG setup

label	company	part no.
lens plan-convex (f=200 mm)	Thorlabs	BK7 AR650-1050 +200
lens plan-concave (f=-75 mm)	Thorlabs	BK7 AR650-1050 -75
SHG BBO Crystal 200 μm	Newlight Photonics	BTC5020-SHG800(I)-AR
THG BBO Crystal 100 μm	Newlight Photonics	BTC5010-THG800(I)-AR
Calcite Time Delay Compensator	Newlight Photonics	TDC12101-AR
Dual Wave Plate $\lambda/2$@800 nm + λ@400 nm	Newlight Photonics	WPD03-H800-F400-SP
Dichroic Mirror HR266	Lasercomponents	HR266HT532+1064/45/AR PP1025UV

In tab.2.2 the main parts for the THG setup are listed. See fig.2.2 for notations and a schematic sketch.

As a collinear alignment was chosen, the alignment of the setup is rather uncomplicated. In a first step a telescope is used to change the beam diameter to match the THG crystal diameter of 5 mm in order to achieve a sufficient conversion efficiency. The telescope consists of a plan-convex lens L1 with a focal length of 200 mm and a plan-concave lens L2 with a focal length of -75 mm, leading to a magnification M of $M = -\frac{-75\,\mathrm{mm}}{200\,\mathrm{mm}} = 0.375$. The distance between the lenses is 200 mm as this is the greater focal length. The alignment of the telescope needs to be checked with the beam profiler as small changes in the divergence of the beam lead to significantly different focal spot sizes. The telescope can be used to change this size on purpose. Note that the beam must hit the curved side of the lenses first so that both sides contribute to the refraction.

The telescope is followed by a Type 1 BBO crystal for SHG. The crystal must be adjusted in a way that the conversion efficiency is maximal, a spectrometer is used for inspection. As the group velocity dispersion for fundamental and second harmonic is different in the materials used, a time delay between the two of them is introduced which needs to be compensated before third harmonic generation takes place. Therefore, fundamental and second harmonic can be separated and a time delay can be introduced by a delay line. An easier approach is not to separate the beams but to use a birefringent calcite time delay compensator. As fundamental and second harmonic have different polarizations, this can be done in our case. Afterwards a special halfwaveplate ($\lambda - \lambda/2$) is used to change the polarization of the transmitted fundamental part to horizontal while the second harmonic part is not influenced. At this point a Nicol prism is used to check the polarization. Con-

sequently a BBO Type 1 crystal for sum frequency mixing is used which merges a 800 nm and a 400 nm photon (both horizontally polarized) into a 266 nm photon with a vertical polarization. Again fundamental and second harmonic come collinear with the 266 nm part. To separate the wavelengths again dicroic mirrors have to be used. (D1-D3) These mirrors have a high reflectivity at 266 nm and a high transmission at 400 nm and 800 nm, see sec.2.1.4. As the available mirrors still reflect a non-negligible part of fundamental and second harmonic, three of these mirrors have to be used. Afterwards the polarization is checked again with the Nicol prism and can be changed by rotating the THG crystal. By monitoring the power at this point, the time delay compensator can be adjusted by tilting and rotating so that the conversion efficiency is at a maximum. The polarization needs to be checked as different settings of the components can lead to high conversion efficiencies but have different polarizations at the end.

The conversion efficiency of the whole THG line was measured for 1 W power in the fundamental and turned out to be approximately 3% at best. For a more detailed description of THG for femsosecond laser pulses in a collinear setup and a more detailed evaluation see Hernrik Enqvists master's thesis. [16]
In the following fig2.4 the spectrum after the three HR266 mirrors (D1-D3) is shown. The central wavelength at the maximum conversion efficiency is 269 nm, see tab.2.5 for more detail.

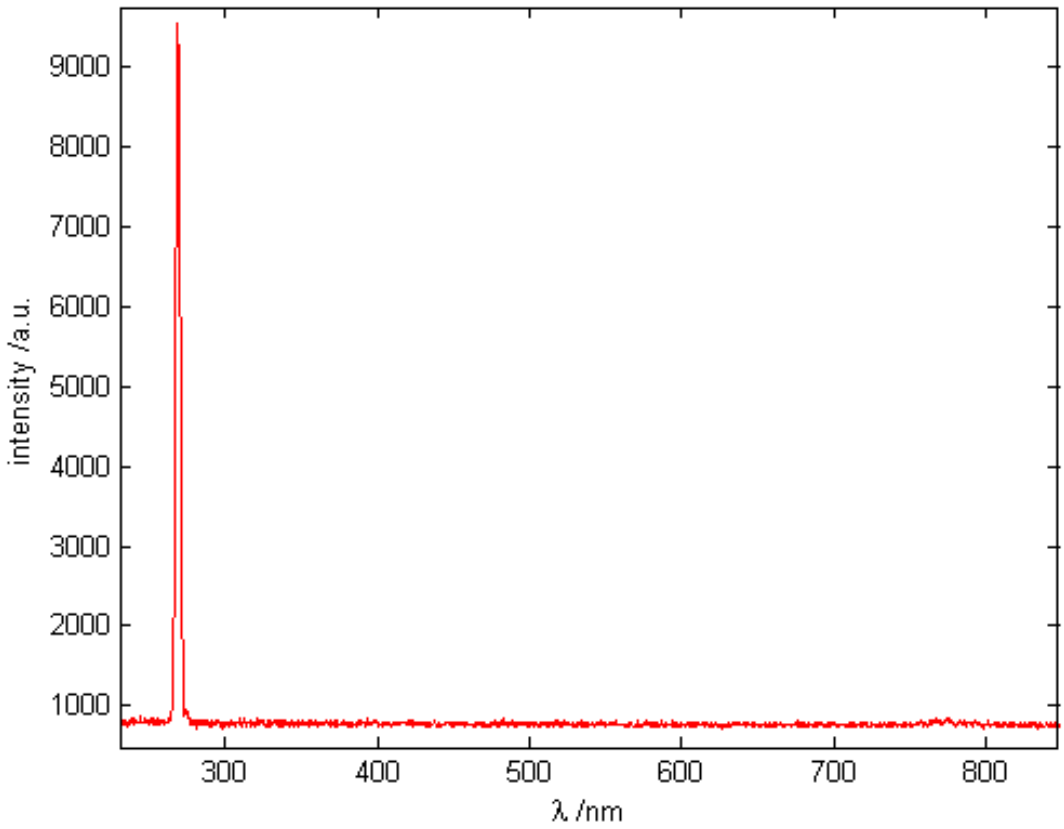

Figure 2.4: Spectrum of the pulses after THG and three dicroic mirrors HR266 (D1-D3).

2.1.4 Dielectric/Dicroic Mirrors

HR800

For 45° reflection of the fundamental, dielectric mirrors with an optimized reflection at 800 nm are used. The part no. is HR800/45 PW1045UV, purchased from Laser-components.
When incident angles different to 45° are inevitable, UV enhanced Al or UV enhanced Ag mirrors have to be used. In the following tab.2.3 the available mirrors in the lab are listed.

Table 2.3: HR800 and UV enhanced Al and Ag mirrors

label	company	part no.
HR800	Lasercomponents	HR800/45 PW1045UV
UV enhanced Al mirror	Thorlabs	PF10-03-F01
UV enhanced Ag mirror	Thorlabs	PF10-03-P01

HR400HT800

The tranmission curve provided by the manufacturer (Lasercomponents) is shown in fig.2.5 for unpolarized light.

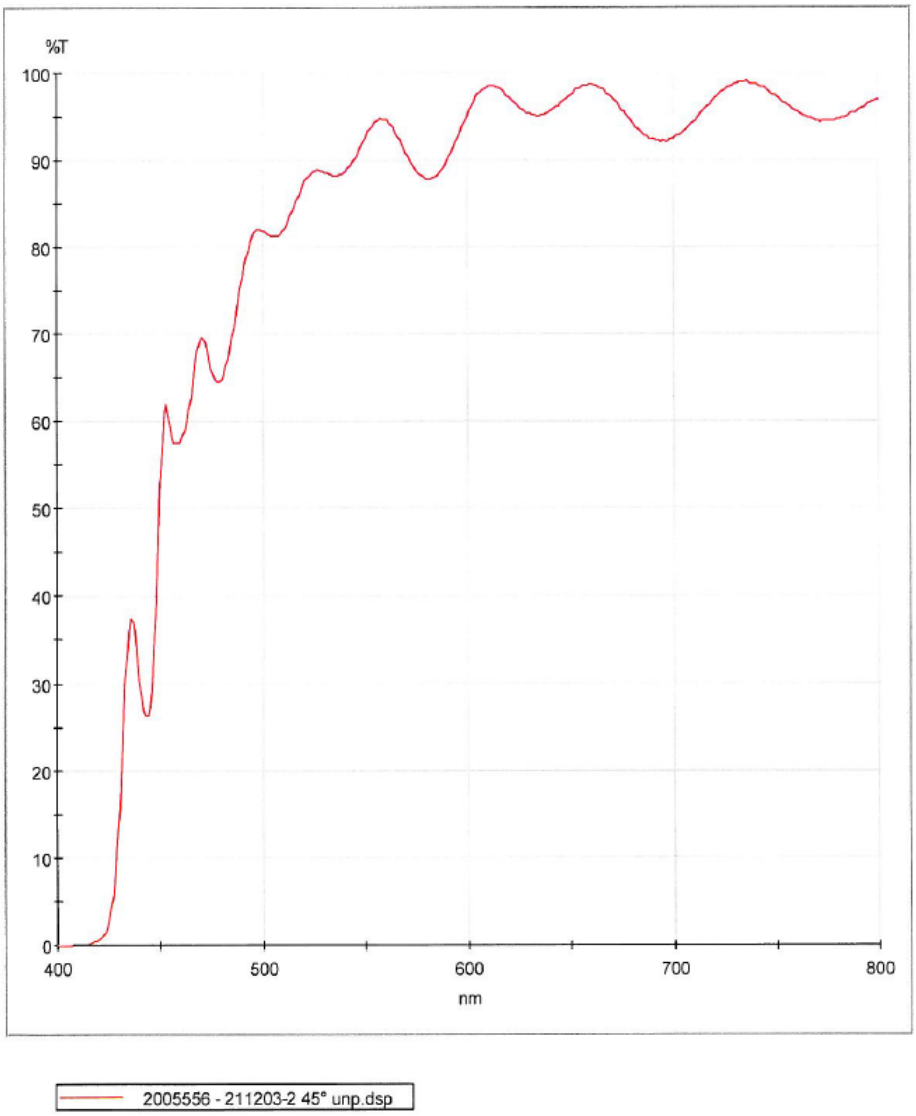

Figure 2.5: Transmission of dicroic mirror HR400HT800.

HR266

By comparing the power of 800 nm, 400 nm and 266 nm right before (P1) and after a dielectric mirror (P2), the reflectivity R of the mirror is measured. Results see tab2.4.

Table 2.4: Reflectivity HR266

wavelength /nm	P1 /mW	P2 /mW	R = P1/P2
800	380	40	0.11
400	76	16	0.21
266	21	20	0.95

All three HR266 mirrors used show the same reflectivity. As the 800 nm and 400 nm part

would be too high after one mirror, three pieces are used in the setup. The specifications provided by the manufacturer of the mirror are shown in fig.2.6. The measured results are clearly different to the specifications which can be caused by different measurement techniques.

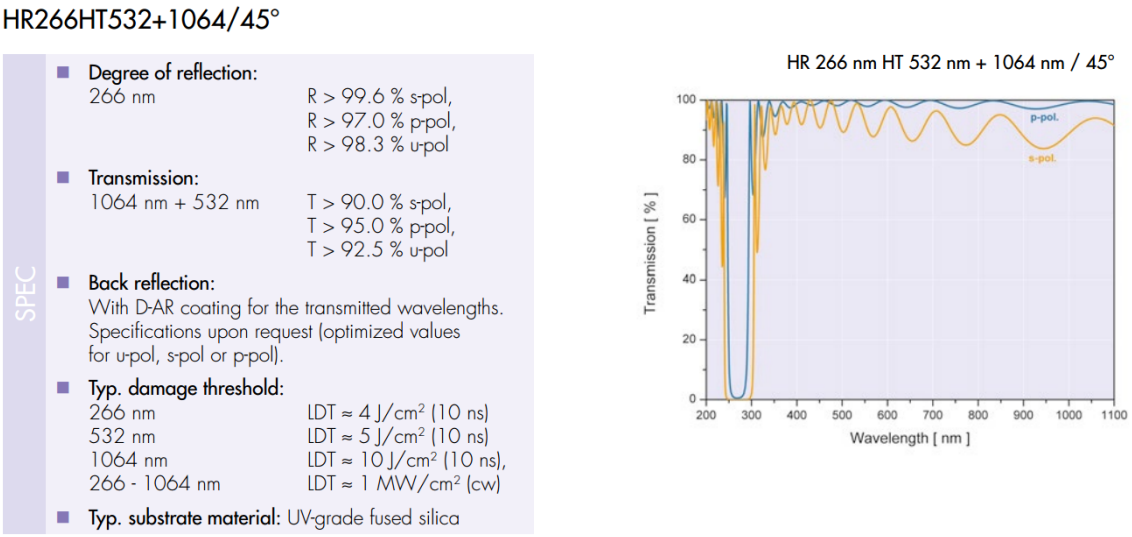

Figure 2.6: Transmission and specifications of HR266[3].

2.1.5 Delay Stage

The delay stage used with the single axis linear motor CONEX-LTA-HS from Newport is moved back and forth in order to in- and decrease the optical path length and thereby manipulating the time delay between pump and probe pulse. The stage can be controlled via Matlab. The travel length is 50 mm with an minimum incremental motion of 0.1 μm and unidirectional repeatability of 0.5 μm. [4]

Alignment

In order to avoid a lateral shift of the beam when the stage moves, the alignment of the stage is of extraordinary importance. To avoid a vertical shift of the beam, the mirror on the stage which gets hit second by the beam is removed. By observing the beam at a

[3] https://www.lasercomponents.com/de/?embedded=1&file=fileadmin/user_upload/home/Datasheets/lco/katalog/beschichtungen/high_pow_longpass_shortpass_mirror.pdf&no_cache=1

[4] http://assets.newport.com/webDocuments-EN/images/LTA_Data_Sheet_MC.pdf

spot far away from the stage while it moves, the mounted mirror is aligned in a way that the spot does not move vertically. Relocate the second mirror and repeat the procedure. To avoid a horizontal shift, the mirrors on the stage must be aligned at 90 degrees relative to each other. Therefore, the same procedure as before is used with both mirrors mounted. For fine adjustments the focal spot is observed at the beam profiler while the stage is moving. Note that even a small beamwalk of only a few μm will cause a loss of spatial overlap leading to false results.
Once the mirrors on the stage are aligned, the stage needs to be fixed with three screws as two are not enough to guarantee stability while the stage is moving.

Control

Via a serial USB port communication with the PC can be achieved. The stage can either be controlled by the supplied graphical user interface or for more complex tasks via Matlab.
Therefore, the number of transmitted bits per second (Baudrate), the number of data bits, stop bits, the parity and the terminator must be specified when the serial USB port is initialized.

Optical Path Length

As the optical path is changed twice as much as the delay stage travels, a optical path length difference of 100 mm is possible. The travel length Δl of the delay stage translates to time delay Δt as follows:

$$\Delta t = 2 \cdot \frac{\Delta l}{c} \tag{2.1}$$

Whereas c is the speed of light.

2.1.6 Counter

The signal from the MCP can be interpreted either by digitizing and subsequent analysis of the data or with the gated photon counter SR400 from Stanford Research Systems which is referred to as counter and acts as a hardware discriminator.
The counter needs the signal from the MCP as well as the trigger from the laser and is able to determine the number of hits in a given time interval with constant discriminator. By

adjusting the Gate Delay and the Gate Width from the counter, hits from different time windows relative to the trigger can be detected. Of course this method is less distinctive but faster than acquiring the whole signal.
The counter is - very similar to the delay stage - controlled by a serial USB port and communication via Matlab.

2.1.7 Beam profiler

A beam profiler camera is used in order to measure the shape and the diameter of the focal spot. The beam profiler is controlled via USB with Matlab. Align the beam profiler at the point where the focal spot has the lowest diameter. In order to align the beam on the CCD chip, open the front of the beam profiler and put a piece of paper right in front of the chip. Use the last mirror before the beam profiler to lay the beam onto the paper and be careful not to hit the chip directly. Lower the power of the beam to the minimum and remove the paper. The beam will saturate the chip but causes no permanent damage. Use the set of optical density filters to attenuate the beam gradually until the chip does not saturate. The provided Matlab function presents the position and the FWHM in 2 dimensions of the focal spot as well as the image of the focal spot, e.g. see fig.2.10
The CCD chip is sensitive to 800 nm, insensitive to 400 nm and cannot detect 266 nm because of an absorbing thin coating on top of the chip. The pixels of the chip translate to length as follows:
Horizontal: 5.6 μm/pixel
Vertical: 5.5 μm/pixel The size of the CCD chip is 640 pixels horizontally and 480 pixels vertically. For more details see Christian Gösweiner's bachelor's thesis. [17]

2.1.8 Single Shot Autocorrelator SSA

The SSA (Hi-Res-SSA) is a commercial product of Coherent. The signal is proportional to the intensity of the signal as a function of time. The autocorrelation signal is detected by a CCD array and can be displayed at the oscilloscope, see fig.2.7. The FWHM of the signal is then proportional to the pulse length. The SSA has a wavelength coverage of 680 nm to 1100 nm and pulse length range from 20 fs to 20 ps with a resolution of 2 fs.
To prevent the SSA from damage, the reflex from a wedge is used for the measurement. The amplitude of the signal at the oscilloscope must not exceed 800 mV. Note that the use of OD filters in order to attenuate the signal leads to false results as the filters stretch

the pulse.

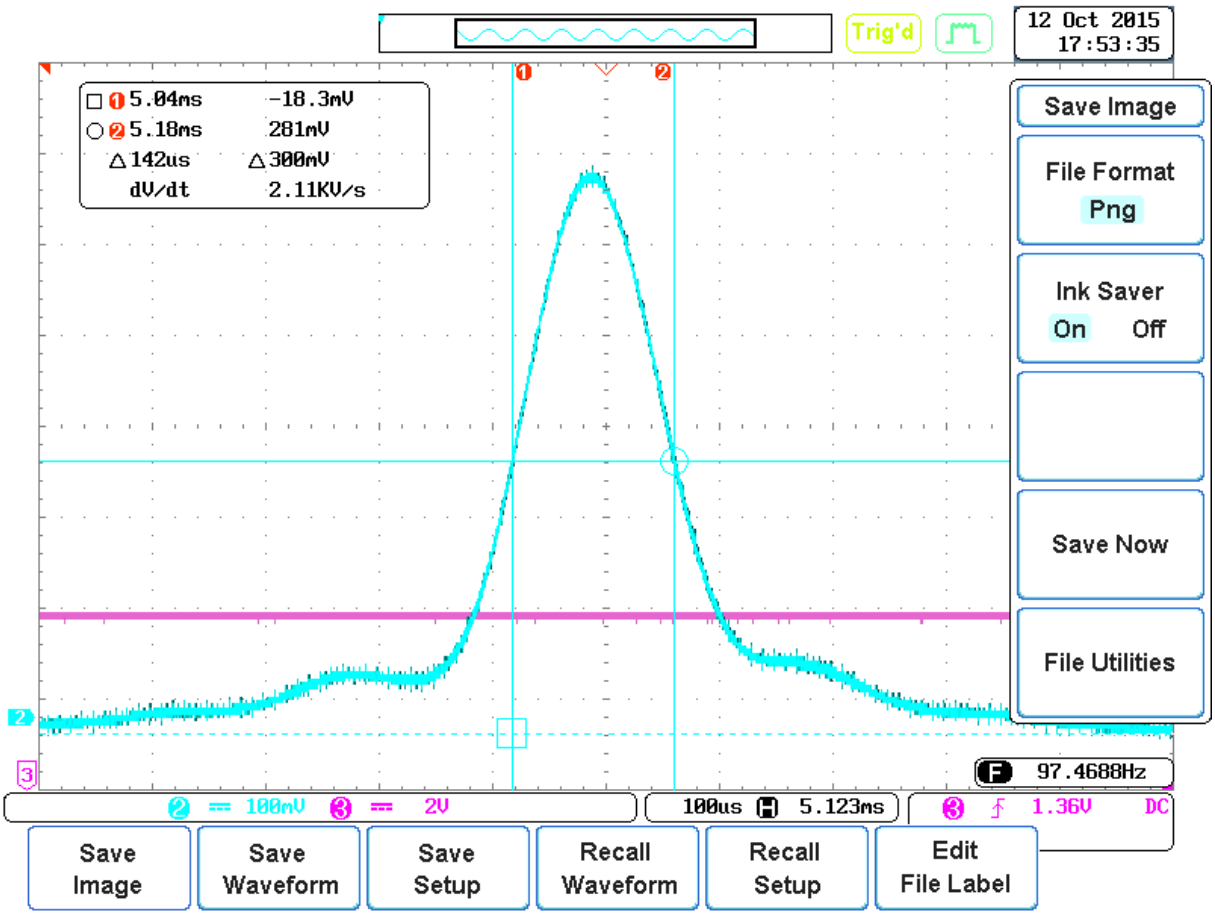

Figure 2.7: Pulse length of 800 nm pulse measured by the SSA. Signal of the SSA for 800 nm pulses. FWHM is 142 μs which corresponds to a pulse length of 21.8 fs

The FWHM in μs measured at the oscilloscope must be multiplied by a factor of $\frac{0.23fs}{1.5\mu s}$ in order to get the pulse length. For the example in fig. 2.7 this results in a pulse length of 21.8 fs. Note that this is the pulse length at the laser output, without any material other than air in the optical path with optimized chirp. By changing the chirp the signal gets broader which means the pulse length gets longer.

2.1.9 Pump-Probe Overlap

A crucial step and probably the most challenging and important one in the construction of the optical setup is to overlap pump and probe pulses inside the spectrometer in space and time. The alignment and stability of the overlap is essential for a succeeding experiment.

2.1.9.1 Overlap in Space

The first step on the way to a stable overlap in the spectrometer is to lay the two beams collinear over each other beginning at the third HR266 (D3). Therefore, the beams are observed alternately on a screen nearby D3 and a screen far away (a distance of a few meters is sufficient). One of the two beams is held constant while the other one is shifted by tilting D2 when the near screen is observed and D3 when the second screen far away is observed. This is done alternately until both beams are at the same spot on both screens which guarantees collinearity.
For a finer adjustment a mirror right after L3 reflects the beams onto the beam profiler which is situated at the position of the minimal diameter of the focal spot. By tilting D3, the beams are aligned exactly over each other.
When the THG setup is in use, the beam profiler will not detect the 266 nm pulses. Therefore, a piece of paper [5] is put onto one of the safety glasses which is then observed with a camera. The safety-glass blocks all other wavelengths from the laser except the fluorescence light resulting from the pulses on the piece of paper. This method is good enough to find the overlap in the spectrometer but is not accurate enough to measure the diameter of the focal spot. Whenever possible the use of the beam profiler should be favoured.

2.1.9.2 Overlap in Time

In order to find the overlap of pump and probe pulse in time (which equals the overlap in space the direction of propagation), the optical paths must be of exact same length. For a rough estimation both paths are built equally long by simply measuring the lengths with a tape measure. Hereby the stage should be considered in the position half way from the lower to the upper maximum. As pulses with different wavelength do not have the same group velocity in a material a time delay is introduced[6].

The calculated time a pulse needs to traverse 4 mm of fused silica is 18.6 ps for 266 nm and 19.1 ps for 800 nm. The time delay is therefore 0.5 ps which does not affect the timing badly. Therefore, the difference in the group velocities can be neglected at this point.

[5] It is recommended to use post-its as they provide a strong effect of fluorescence.

[6] See M. N. Polyanskiy. "Refractive index database," http://refractiveindex.info for optical constants of materials used.

A finer adjustment is done by using the photodiode. The photodiode is connected to the oscilloscope, the beams are blocked and a scatter of each will be detected consequently. The power of the beams must be adjusted in a way that the amplitudes of the signal at the oscilloscope are the same. For both beams the point at the rising edge where it has half the amplitude is determined. The difference in time between these two points is a good estimation for the time delay of pump and probe. The optical paths are adjusted until pump and probe seem to be detected at the same time. Herby the delay time can be estimated within an uncertainty of tens of picoseconds. In order to find the exact point where the time delay is zero, the two beams are focused into the spectrometer and a signal is acquired. 20 to 100 cps for pump only and probe only is sufficient for this purpose. When the stage is moved back and forth, the countrate will rise drastically when the two pulses overlap see fig.2.9. The Matlab program timescan_counts_2gates.m will perform an automatic search. Hereby the scan window and the step size for need to be specified. The stage moves a stepsize and the ion yield is acquired by the counter. The gates at the counter can be used for an ion mass selective measurement.
It is important to obsere the countrate at all times in order to prevent the MCP from any harm due to high countrates. The stage must be moved in steps of approximately 50 fs (depending on the used wavelengths and pulses) in order to resolve the overlap.

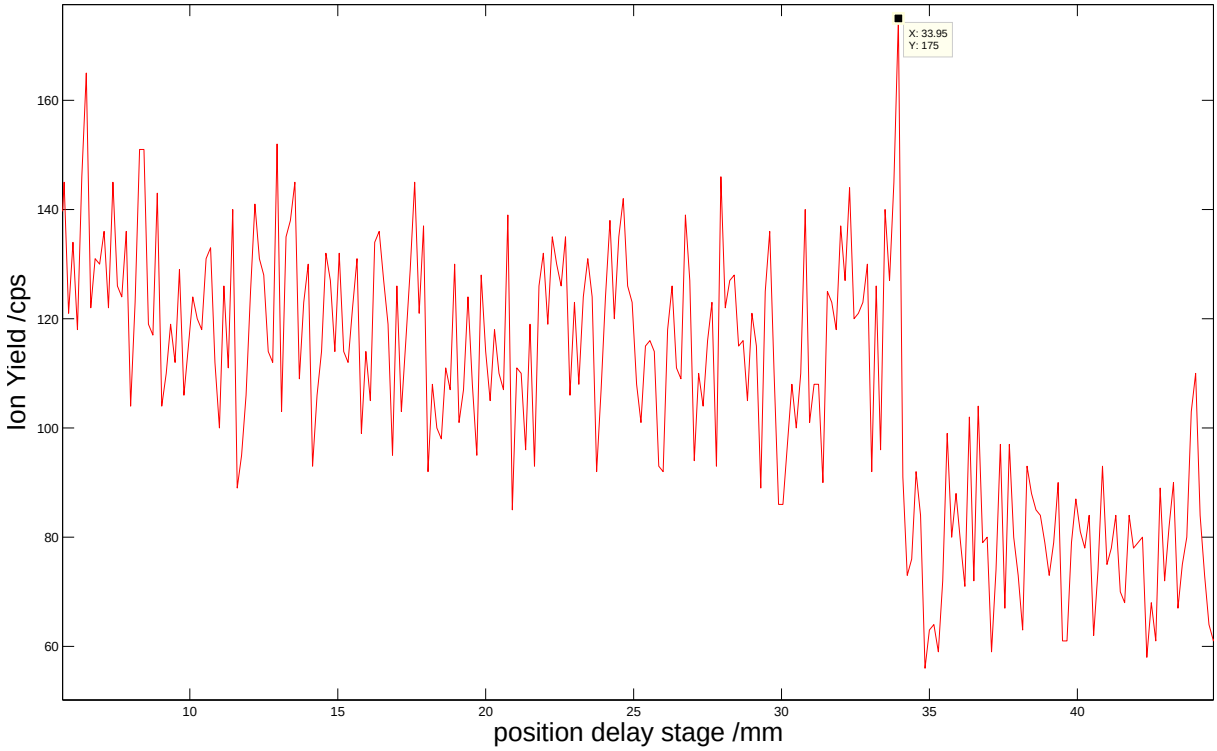

Figure 2.8: Rough timescan with $5 \cdot 10^{-6}$ mbar acetone, 266 nm: 11 mW, 800 nm: 17 mW.

In fig.2.8 a rough scan over the whole travel length of the delay stage is shown. At approximately 33.95 mm the two pulses overlap. For positions lower than that, the pump pulse comes before the probe - referred to as pump-probe -, excites the molecules and leads in combination with the probe pulse to a higher ion yield compared to the opposite case. For positions greater than 33.95 mm the probe comes first and does not excite acetone molecules therefore the ion yield equals the yield of pump only plus probe only - this case is referred to as probe-pump. The difference in the countrates between pump-probe and probe-pump is approximately 40 cps which equals 50% of the probe-pump yield. Note that fig.2.8 shows the best possible outcome of such a scan. The difference in the ion yield between pump-probe and probe-pump is remarkably high and visible for the whole travel length of the delay stage and additionally the overlap itself can be seen. For a better signal-to-noise ratio the integration time at the counter can be increased but will cause longer measurements. An integration time of 0.5 s is sufficient for rough scans.

A more detailed scan reveals the structure of the overlap see fig.2.9.

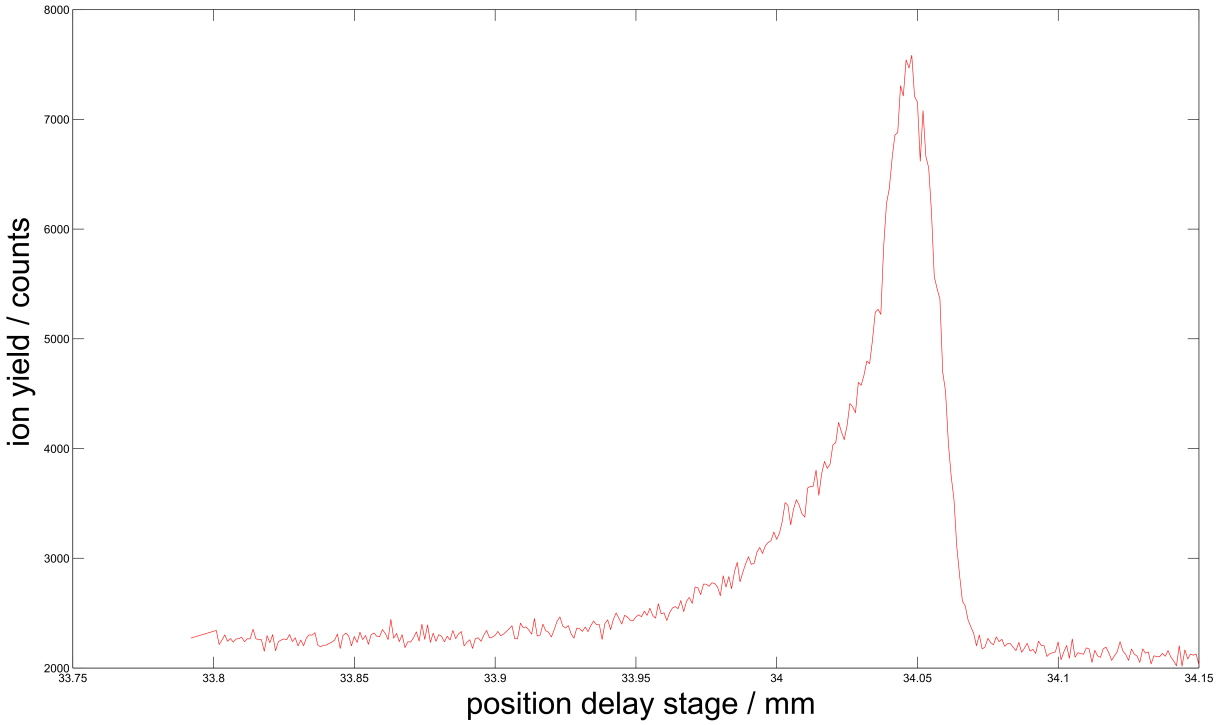

Figure 2.9: Detailed timescan with $5 \cdot 10^{-6}$ mbar acetone, 266 nm: 22 mW, 800 nm: 15 mW.

The exact time-zero in this case where the two pulses overlap in time is at a position of 34.05 mm. The asymmetry of the signal results from excitation and relaxation of the acetone molecules. Without stable or metastable states which can be populated by pump or probe, the signal would be symmetric. The FWHM of such a signal is called apparatus response and can be used to estimate the upper limits of the the pulse lengths of pump and probe as it consists of the convolution of the two pulses. See fig.2.15 for an example.

Once the overlap is found the spacial overlap can be optimized at the time-zero point by maximising the signal.

Typically the search for the time-zero can become tedious even if the spatial overlap was optimized beforehand. An improvement would be to install a target e.g. a card which can be brought into the focus directly in the spectrometer. This way one could make sure that the pulses overlap in space where they should. The overlap at the beam profiler outside of the spectrometer is only a good guess.

2.1.10 Size and Intensity of the Laser Beams

In order to estimate the intensity of the pulses, in addition to the pulse length, the size of the focal spots must be measured. Therefore, the beam profiler is in use. Note that the following examples in fig.2.10 and fig.2.12 vary from experiment to experiment as the size can be adjusted by the telescope (L1, L2) to fit the experiment.

800 nm

The size (FWHM) of the focal spot at the camera is 56 μm in horizontal and 71.5 μm in vertical direction. The focal spot is not perfectly symmetric which is most likely caused by some small misalignment of the beam at the lense (L3) and the fact that the output beam of the laser itself is not perfectly symmetric as well. For calculations a mean focal diameter of 64 μm is used.

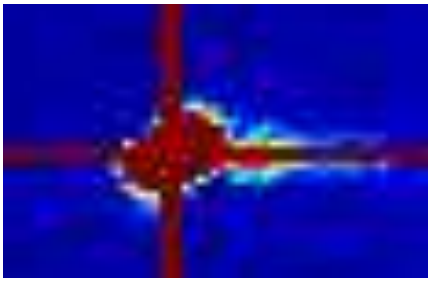

Figure 2.10: Focal spot of the 800 nm pulses, imaged with the beam profiler. Red lines cross where the maximum of the intensity occurs.

As the pulse length of the 800 nm pulse was measured by the SSA, the intensity of the pulses can be estimated as follows:

$$I = \frac{P}{f_{\text{rep}}(D/2)^2\pi\tau} \tag{2.2}$$

I...Intensity /$\frac{\text{W}}{\text{cm}^2}$
P...mean power of the beam /W
f_{rep}...repetition rate of the laser = 3 kHz
D...diameter of the focus /cm
τ...pulse length /s

The pulse length of the 800 nm pulse was estimated to be 35 fs, the mean diameter is 64 μm. For a mean beam power of 35 mW this leads to an intensity of 10 $\frac{\text{TW}}{\text{cm}^2}$. Considering the uncertainty in the pulse length, the size of the focal spot and given the fact that the estimation is simplified, a uncertainty of several 10% is estimated.

Another method to estimate the intensity is to make use of the shift of above-threshold-

ionization (ATI) peaks corresponding to the ponderomotive energy U_p which depends linearly on the intensity I.

This can be written as a function of the intensity I and the wavelength λ.

$$U_p = \frac{e^2 I \lambda^2}{8\pi^2 \epsilon_0 c^3 m_e} \propto I\lambda^2 \tag{2.3}$$

m_e... electron mass ($9.11 \cdot 10^{-31}\,\mathrm{kg}$)
e... electron charge ($1.60 \cdot 10^{-19}\,\mathrm{C}$)
c... vacuum speed of light ($3 \cdot 10^8\,\mathrm{m/s}$)
λ... wavelength

Whereas the intensity depends linearly on the power:

$$I = c_1 P \tag{2.4}$$

c_1...constant $/\frac{1}{\mathrm{cm}^2}$

Which leads to:

$$U_p = c_1 P \frac{e^2 \lambda^2}{8\pi^2 \epsilon_0 c^3 m_e} \tag{2.5}$$

As U_P depends linearly on the power, the shift of an ATI peak due to the shift of U_P with power can easily be used to estimate the constant c_1 connecting power to intensity.

$$\Delta U_p = c_1 \frac{e^2 \lambda^2}{8\pi^2 \epsilon_0 c^3 m_e} \Delta P \tag{2.6}$$

ΔU_p...shift of an ATI peak
ΔP...difference in power

$$c_1 = \frac{\Delta U_p}{\Delta P} \frac{8\pi^2 \epsilon_0 c^3 m_e}{e^2 \lambda^2} \tag{2.7}$$

Electron energy measurements on xenon eiTOF_0314 with a power of 15 mW and eiTOF_0324 with a power of 60 mW led to a shift of the ATI peaks of $\Delta U_p = 0.8\,\mathrm{eV}$ see fig.2.11. This leads to $c_1 = 2.98 \cdot 10^{14} \frac{1}{\mathrm{cm}^2}$. E.g. 35 mW power corresponds to an peak intensity at the focus of about $10.5\,\frac{\mathrm{TW}}{\mathrm{cm}^2}$ which is in good agreement with the estimated intensity of $10\,\frac{\mathrm{TW}}{\mathrm{cm}^2}$ with the simple approach above. Considering the uncertainty in power of the laser beam and the exact position of the ATI peaks a uncertainty of a few 10% seems reasonable.

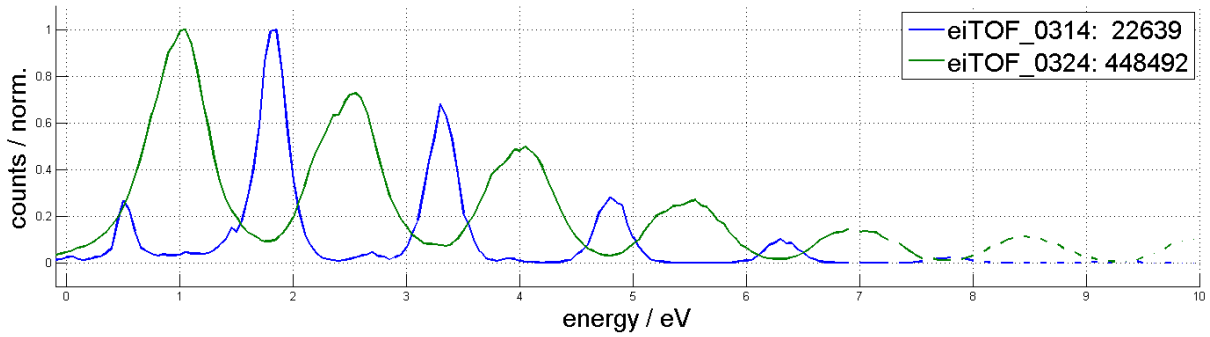

Figure 2.11: Xenon Electron Energy Spectrum 800 nm. eiTOF_0314 with a power of 15 mW and eiTOF_0324 with a power of 60 mW

400 nm

The size (FWHM) of the 400 nm focal point is in this case approximately 90 μm in each direction.

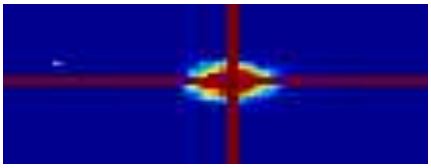

Figure 2.12: Focal spot of the 400 nm pulses, imaged with the beam profiler. Red lines cross where the maximum of the intensity occurs.

As the pulse duration of the 400 nm and 266 nm pulse can not be measured with the SSA, just the appartusresponse of the pump-probe measurements on acetone give an idea about the pulse length. The intensity can not be determined this way. The same goes for the U_p shift as for 400 nm pulses the shift is too low to resolve.

266 nm

The beam profiler cannot be used for the 266 nm pulses as the remaining 800 nm and 400 nm part dominates the output. The measured focal point is not the 266 nm pulse itself but is proportional to it.

Fig.2.13 shows two focal points of the 266 nm pulse which with a spacing of approximately 600 μm. This structure can not be explained by some reflection because it cannot be blocked separately after the THG but before the THG setup by blocking different parts of the fundamental beam. This strange behaviour must have something to do with the THG setup, the exact reason could not be found. The second focal point does not matter for pump-probe measurements as only one of them has spatial overlap with the probe

pulse.

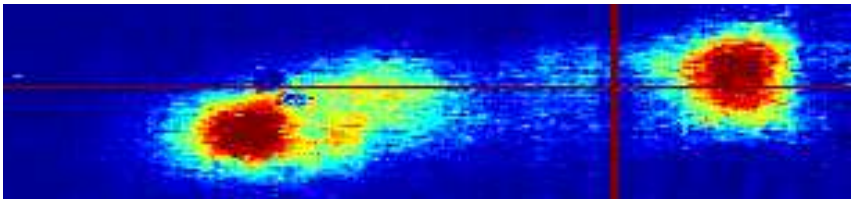

Figure 2.13: Two focal spots of the 266 nm pulses, imaged with the beam profiler. Red lines cross where the maximum of the intensity occurs.

2.1.11 Spectra of Fundamental, SHG and THG Pulses

In the following table 2.5 the central wavelengths as well as FWHM of the used pulses are shown. The spectra were acquired with a spectrometer from Ocean Optics namely USB4000 which has a range from 200 μm to 2000 μm. The 800 nm spectrum shown in fig.2.14 was acquired with an internal spectrometer of the laser system.

Table 2.5: Fundamental, SHG, THG specifications

Fundamental				
	/nm	/eV	/Hz	/cm^{-1}
central wave length	800	1.55	$3.75 \cdot 10^{14}$	12500
FWHM	80	0.16	$3.75 \cdot 10^{13}$	1253
SHG				
	/nm	/eV	/Hz	/cm^{-1}
central wave length	405	3.06	$7.40 \cdot 10^{14}$	24691
FWHM	14	0.11	$2.56 \cdot 10^{13}$	854
THG				
	/nm	/eV	/Hz	/cm^{-1}
central wave length	269	4.61	$1.12 \cdot 10^{15}$	37175
FWHM	4	0.07	$1.66 \cdot 10^{13}$	553

By assuming Gaussian-shaped pulses without any chirp, the transform limited pulse length can be calculated, see tab.2.6.

Table 2.6: Transform limited pulse length.

	min. pulse length /fs
Fundamental	12
SHG	17
THG	27

For the 800 nm fundamental pulses the pulse length can be measured with the SSA

see sec.2.1.12. The measured pulse length is 21.5 fs which is clearly above the transform limited pulse length of 12 fs. The deviation is not a surprise as the assumption of ideally shaped pulses without chirp does not hold perfectly. An inverse fast-fourier-transformation was done on the spectrum with a software provided by coherent where a pulse length of 25.6 fs was calculated which is in good agreement with the measured pulse length. This again highlights the fact that the pulse shape is not Gaussian.

For the SHG and THG pulses there is no direct method to measure the pulse length available. A powerful technique to measure pulse characteristics such as pulse length, intensity and the optical spectrum as well as the spectral phase is FROG which is short for frequency-resolved-optical-gating.

A cross-correlation measurement of the pump-probe instrumental response on xenon with THG pump and SHG probe revealed a FWHM of 120 fs which leads to the assumption that the pulse lengths of SGH and THG are well above 17 and 27 fs respectively. This is not only due to the pulse form but also to the material through which the pulses have to traverse before entering the spectrometer.

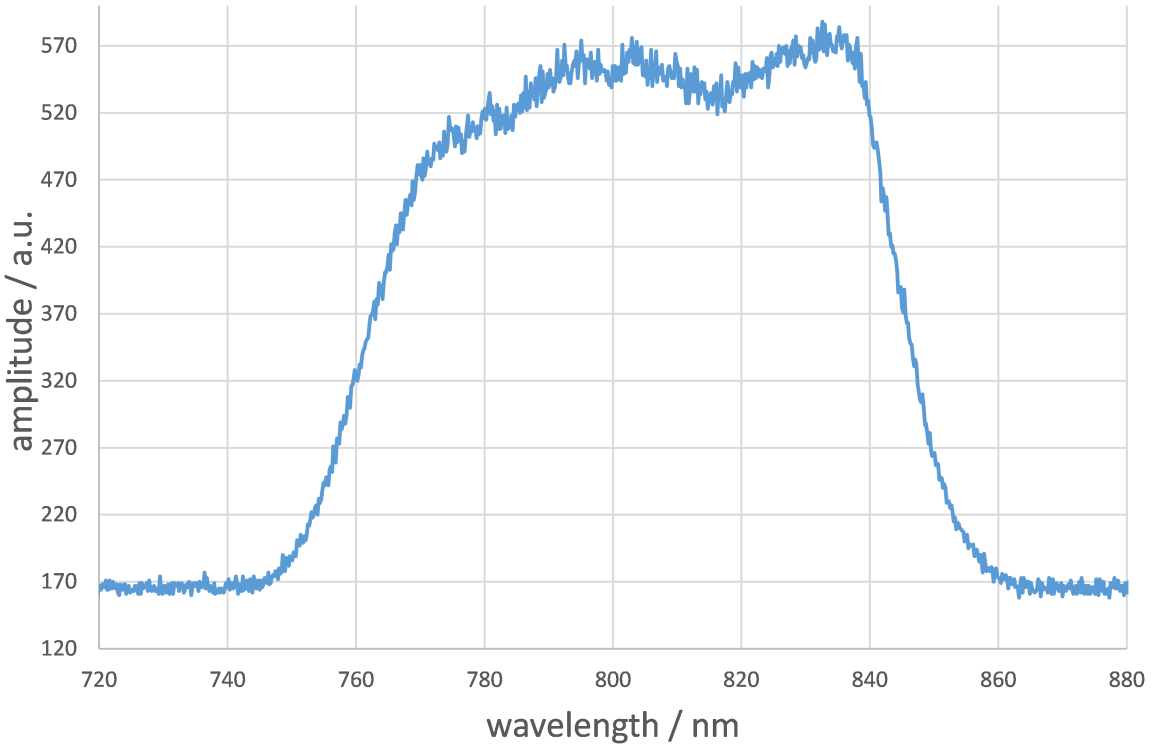

Figure 2.14: Spectrum of the fundamental 800 nm pulse.

2.1.12 Chirp

The chirp of the pulses has clearly a large influence on the pulse duration and pulse shape and consequently on the conversion efficiency in the non-linear crystals as well as on the intensity of the focal point. Therefore, a proper adjustment of the chirp is crucial for the setup. As the chirp can only be regulated by a continuous control mechanism without a scale, it was not possible to quantize the chirp.

2.1.12.1 Match Chirp in Pump and Probe Path

As there is just one chirp adjustment for both pump and probe path, the used materials in both paths must induce the same amount of linear chirp which can be compensated. Therefore, it may be necessary to put additional material (BK7, fused silica) in one of the paths, preferably before non-linear processes as SHG and THG take place. The apparatus response is hereby the quantity to look at. As glass is put into one path the response will change, for the setting the chirp has to be optimized with regard to the apparatus response. By simply trying different settings the optimum amount of additional material can be found. There is no straight forward way to do so, the optimization can get tedious. For a more exact, continuous and faster adjustment, wedges with a small wedge angle of a few degrees should be purchased.

For 266 nm pump 400 nm probe experiments, 2 mm of glass are necessary in the probe path. The minimum apparatus response for acetone turned out to be 124 fs see fig.2.15. Without optimization the response is about 170 fs. This illustrates the necessity of this optimization as the pulse length and subsequently the response time determines the time resolution of the experiment.

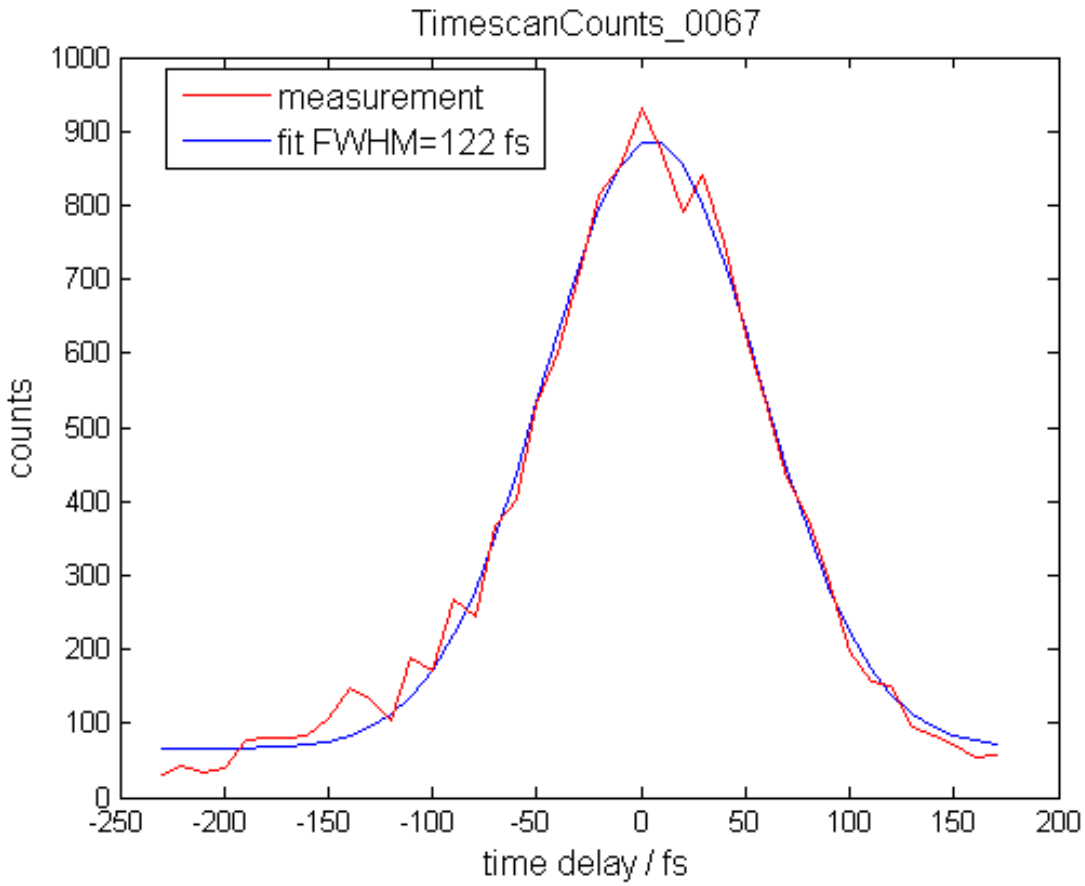

Figure 2.15: Optimized apparatus response of acetone, 4 mW, 266 nm pump; 17 mW, 400 nm probe.

2.1.12.2 Estimation of linear Chirp

In the following equation 2.8 the pulse length t_{out} of a pulse with the initial length t_{in} is shown. GDD is the abbreviation for group delay dispersion which is the group velocity dispersion (GVD) times a length. Note that this equation only holds for a transform limited Gaussian pulse without chirp which is an unrealistic scenario.[7]

$$t_{out} = \frac{\sqrt{t_{in}^4 + 16(ln(2))^2 GDD^2}}{t_{in}} \tag{2.8}$$

In the following tab.2.7 the GVD (which is GDD/mm) for the most used materials in the lab are given. Note that BK7 is opaque for 269 nm pulses.

[7] An excellent overview about the influence of chirp on ultrashort pulses is provided by `https://www.newport.com/the-effect-of-dispersion-on-ultrashort-pulses` and `http://www.coherent.co.jp/document/docs/PropagationDispersionMeasurement_of_sub_10fsPulses.pdf`

Table 2.7: Refractive index n and GVD for fused silica, BK7 and CaF_2. [8]

λ / nm	n	GVD /fs^2/mm
Fused Silica		
269	1.4984	193
405	1.4696	96
800	1.4533	36
BK7		
405	1.5302	120
800	1.5108	45
CaF_2		
269	1.4612	125
405	1.4415	66
800	1.4305	27

Using eq.2.8 and values from tab.2.7 we are able to calculate the pulse broadening. E.g. when a 800 nm pulse with a pulse duration of 25 fs gets through 10 mm of fused silica the outcoming pulse length is 40 fs. As a typical lens is approximately 4 mm thick this is a realistic scenario for the whole setup. As there is no direct method to measure the pulse length of anything other than the 800 nm pulse, the pulse broadening can not be calculated as the output pulse length depends heavily on the incoming pulse length.
In general fused silica and BK7 are acceptable materials to use in an optical setup. CaF_2 is of course the better choice but not always available. The pulse broadening due to GVD can be fully compensated by compensated by pre-chirping the pulse. The higher order distortions can theoretically be compensated with big amount of experimental effort. (coherent

2.1.12.3 Compressor drift

A problem of the setup is that the optimal chirp changes during the first hours after the system is switched on. In order to quantize the drift, the pulse length on the SSA was measured.

The chirp was optimized for minimal pulse length on the SSA which led to a pulse length of 22 fs. 80 minutes later the pulse length changed to 31 fs in combination with a beam walk of about 1 cm on a distance of 6 m. The chirp was optimized again leading to a pulse length of 23 fs. Another 20 minutes later it went up to 24 fs which could be changed back to 23 fs. After that the chirp seemed stable.

[8] values taken from`http://refractiveindex.info/?shelf=main&book=CaF2&page=Malitson`

In conclusion the system is not ready for measurements or finer adjustments until it is thermally stable which seems to be the case earliest 2 hours after switching it on.

2.1.13 Evaluation Optical Density (OD) Filters

A set of neutral density filters is available in the lab in order to attenuate the signal. They are used for the beam profiler as well as for the photodiode in order to avoid damage. See tab.2.8. The optical density OD is defined by the following equation:

$$OD = log_{10}\left(\frac{1}{T}\right) \tag{2.9}$$

whereas T is te transmission.

Table 2.8: Available OD filters in the lab.

label	company	part no.
OD1 filter	Thorlabs	NE10B
OD2 filter	Thorlabs	NE20B
OD3 filter	Thorlabs	NE30B

The transmission of the filters is highly wavelength dependent see fig.2.16

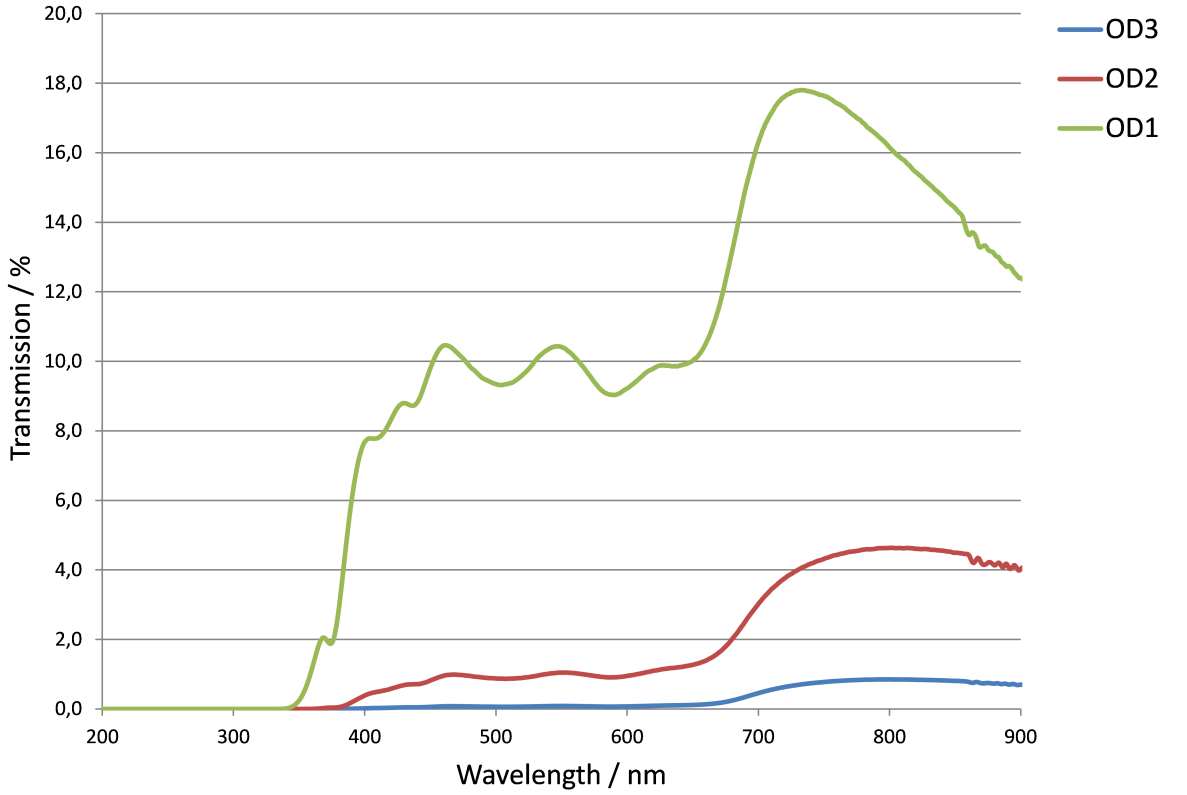

Figure 2.16: Transmission coefficients over wavelength for OD1, OD2 and OD3 filters as provided by the manufacturer.

Therefore, the filters have a lower optical density for the 800 nm pulses as one would expect from the label, values at 800 nm see tab.2.9. By a rather tedious comparison of signals from the photodiode obtained with filters with a certain reflectivity and the available OD filters in the lab, the transmission was determined, results see tab.2.9.

Table 2.9: Transmission and optical density of available filters provided by Thorlabs and measured transmission.

label	$\mathbf{transmission_{Thorlabs}}$ / %	OD / 1	$\mathbf{transmission_{measured}}$ / %
OD1 filter	16.2	0.8	23.0
OD2 filter	4.6	1.3	8.0
OD3 filter	0.9	2.0	1.2

The measured values are higher than the expected ones. Not only is there a uncertainty because the signal height was used to compare the results which is delicate because of the non-linear connection of the signal height with the power. Also Thorlabs used most likely cw-lasers while the measured transmissions in our case are acquired using femtosecond pulses. It is very likely that the transmission will increase for pulses as there is a satu-

ration effect in the material. Therefore, reflectivity filters should be favoured for future purchases regarding attenuation of pulses.

2.1.14 Contrast Main-/Prepulse

For internal reasons of the laser system there is a pre- a main- and a post-pulse separated by a few nanoseconds. Herby the main pulse must overshadow the other two pulses in order to guarantee high quality of the pulses. The ratio of the amplitude of main- to pre-pulse (further referred to as contrast) is the quantity to look at.
Therefore, the photodiode in combination with a suitable set of attenuation filters is used see sec.2.1.13.
For reference the value of the contrast measured by Dr. Podlipensky (service technician from Coherent) in the first week of march 2016 is used which turned out to be 2700.
The values were measured using the reflex of the 800 nm beam at a wedge where only around 4% of the power is reflected. Hereby it is important to use the reflex as the transmitted part will have more chirp. The measurement turned out as folows:
For the main pulse one OD1, OD2 and one OD3 filter was used which led to a amplitude of 43 mV. For the pre- pulse one OD1 filter was used, the amplitude as 16 mV. Using the measured transmissions from tab.2.9 the contrast turns out as follows:

$$\text{contrast} = \frac{\text{amplitude of main pulse}}{\text{amplitude of pre pulse}} = \frac{43\,\text{mV}}{16\,\text{mV}} \cdot \frac{0.230}{0.230 \cdot 0.012 \cdot 0.080} = 2800$$

The difference in the values for the contrast results not only from uncertainties in the transmission determination of the OD filters, but also because the peak value on the PD was not the same for main and pre-pulse. This is because not enough different filters were available in order to tune the transmission. As the signal of the PD will not increase linear with intensity, this can lead to a different contrast. The measured value is the benchmark for future contrast measurements. Note that both values are measured directly after the contrast was optimized.

2.2 Data Analysis

On pump-probe PEPICO experiments, the influence of the pump only and probe only has to be subtracted from the pump-probe spectra. This may seem trivial but appears to be a problem with regard to the way the spectra are obtained from the measurements. There are basically two methods, one called covariance method where the covariance for ion masses in combination with electron energies is calculated see 2.2.1, and one called coincidence method where only time traces with exactly one ion hit and one electron hit are used. An intuitive approach is to subtract the pump only and probe only spectra from the pump-probe spectrum in order to obtain signal resulting just from pumped population of the investigated species. It is not clear whether this approach is reasonable or leads to significant errors. See detailed discussion in the following sections.
For a detailed description of how spectra are calculated from the signals and details about the covariance method see Markus Bainschab's master's thesis [12].

2.2.1 Covariance Method

For a detailed explanation of the covariance method see ref. [18]. In the following equation 2.10 the formula for covariance is given in principle [18].

$$\begin{aligned} Cov(x,y) =& < X(x)Y(y) > - < X(x) >< Y(y) >= \\ & \frac{1}{N}\sum_{i=1}^{N} X_i(x)Y_i(y) - \left[\frac{1}{N}\sum_{i=1}^{N} X_i(x)\right]\left[\frac{1}{N}\sum_{i=1}^{N} Y_i(y)\right] \end{aligned} \tag{2.10}$$

Where $X_i(x)$ is the number of electron-hits in laser pulse i at flight-time x and $Y_i(y)$ the number of ion-hits in laser pulse i at flight-time y. This results in a 2 dimensional covariance matrix. By summing over a certain ion mass (which equals a certain flight-time window) in this matrix, the number of dimensions is reduced to 1 and the electron energy spectrum for a specific ion mass is obtained.

$$I(x) = \sum_{y=y_1}^{y_2} Cov(x,y) \tag{2.11}$$

Where I(x) is the intensity at energy x resulting just from ion masses corresponding to flight-times between y_1 and y_2. First of all this leads to the question if the binning before the covariance matrix is calculated has an influence on the energy spectra. As the ion

masses as well as the electron energies are calculated from the time of flight, a rebinning from time to mass/energy is mandatory at some point. As the appearing summations are independent of each other, they can be exchanged. See eq.2.12.

$$I(x) = \sum_{y=y_1}^{y_2} Cov(x,y) = \sum_{y=y_1}^{y_2} \left(\frac{1}{N} \sum_{i=1}^{N} X_i(x) Y_i(y) - \left[\frac{1}{N} \sum_{i=1}^{N} X_i(x) \right] \left[\frac{1}{N} \sum_{i=1}^{N} Y_i(y) \right] \right) \\ \frac{1}{N} \sum_{i=1}^{N} \left(X_i(x) \sum_{y=y_1}^{y_2} Y_i(y) \right) - \left[\frac{1}{N} \sum_{i=1}^{N} X_i(x) \right] \left[\frac{1}{N} \sum_{i=1}^{N} \sum_{y=y_1}^{y_2} Y_i(y) \right] \tag{2.12}$$

Here $\sum_{y=y_1}^{y_2} Y_i(y)$ can be interpreted as the binning done before the covariance matrix is calculated. As the sums are exchangeable the summation over ion masses can be done at any point without influencing I(x). In conclusion the binning does not influence the spectra.

Another important question is whether covariance spectra from different measurements with different settings (e.g. wavelength, intensity, pressure, time delay) can be compared to each other and subtracted from each other. As the influence of the pump only and probe only signal has to be eliminated in pump-probe spectra by subtracting the only spectra, this is a crucial step.
The main question is whether the higher countrates in pump-probe measurements lead to a different scaling of the obtained covariances, even if the underlying only spectra are not changed. As the first term in the covariance is not simply linear its possible that the different countrates and different open channels do not add linearly to the spectrum in the pump-probe case.
A mathematical proof was not found at this point so measurements for comparison were performed. Therefore, a measurement with the probe coming well before the pump was done. As the probe does not trigger dynamics in acetone, the measurement should give the same result as the addition of a pump only and a probe only spectrum.
A pump power of 13 mW and a probe power of 43 mW lead to a mean ionisation rate of 1.6 $\frac{\text{events}}{\text{pulse}}$ for pump-probe (spectrum see fig.2.17), 1.3 $\frac{\text{events}}{\text{pulse}}$ and 0.4 $\frac{\text{events}}{\text{pulse}}$ for pump and probe respectively at a pressure of $5 \cdot 10^{-6}$ mbar acetone. The only spectra were subtracted from the probe-pump spectrum, see fig.2.18

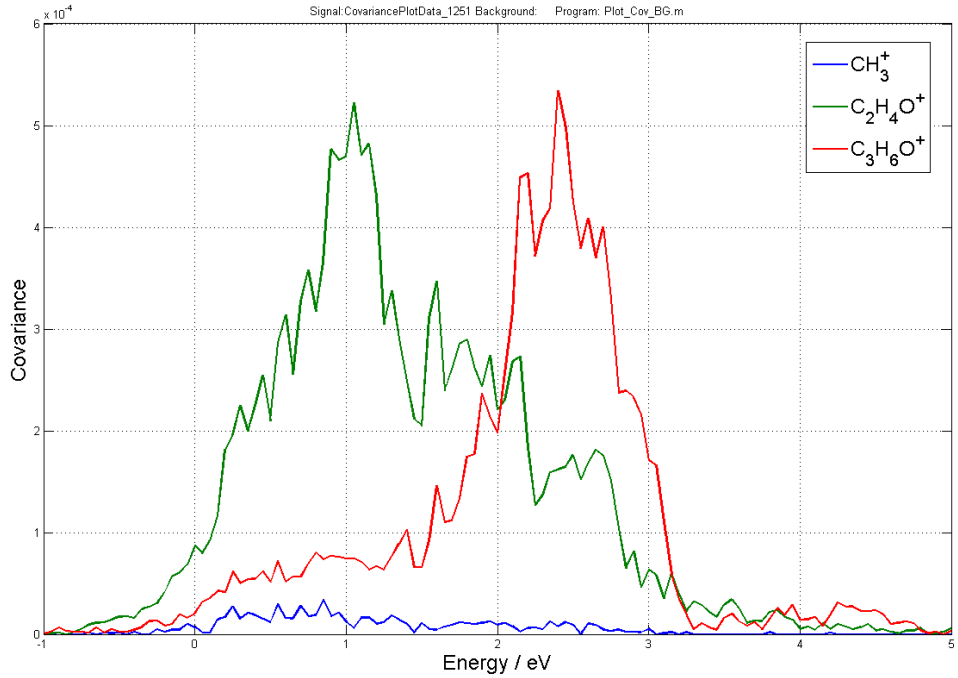

Figure 2.17: Probe-pump spectrum, $5 \cdot 10^{-6}$ mbar acetone, pump power 43 mW, 266 nm; probe power 13 mW, 400 nm.

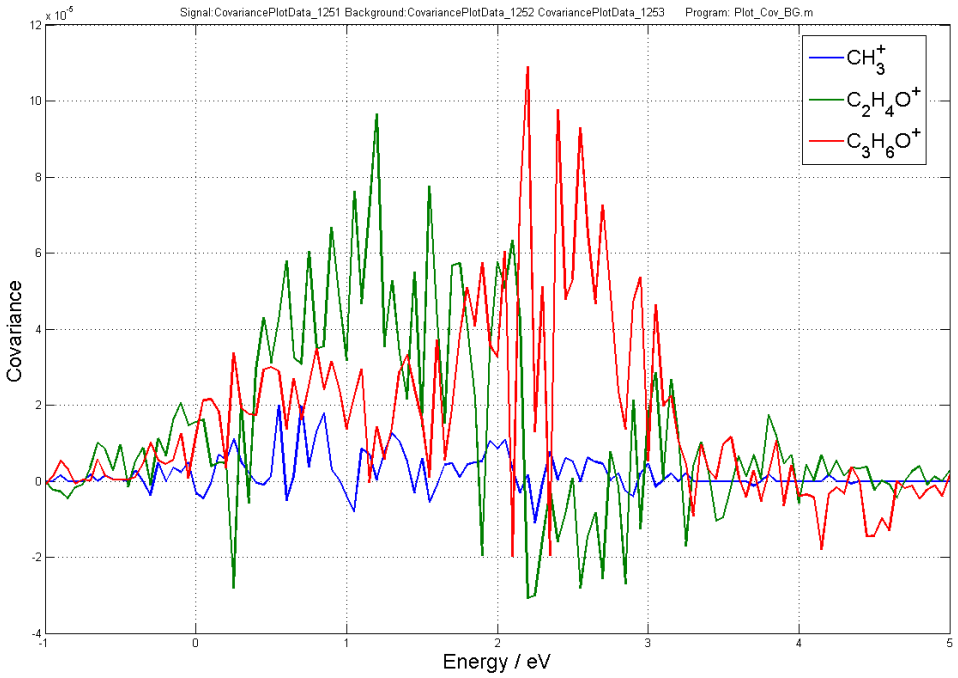

Figure 2.18: Covariance PEPICO spectrum of acetone acquired by subtraction of pump- and probe-only spectra from an probe-pump spectrum. $5 \cdot 10^{-6}$ mbar acetone, pump power 43 mW, probe power 13 mW.

As the remaining signal is a magnitude lower than the non-subtracted spectra and there-

fore probe-pump and the probe only and pump only combined lead to approximately the same result, the subtraction seems to be reasonable. This is of course no proof but affirms the method.

Another idea is to go to such low countrates that coincidence evaluation can be done on the same measurement in order to compare the results. This does not proof anything as for low countrates the first term in the covariance eq.2.10 consists almost only of pulses were one electron is detected with one ion as the probability for the detection of more than one ion and/or more than one electron is low - exactly the same thing the coincidence method depends on. For low countrates the two methods are equal and lead to the same results automatically.

A set of simplified numerical examples did not lead to a clear conclusion as the construction of data is rather delicate. In conclusion the subtraction/summation of covariance signals from different measurements seems to provide reasonable results and therefore can be used for routine measurements. Further research should be done on this topic.

2.2.2 Coincidence Method

For a detailed explanation of the coincidence method see ref. [19]. In contrast to the covariance method where the whole signal is used to obtain the spectra, the coincidence method makes use only of the pulses where exactly one ion is detected in coincidence with exactly one electron.

As there the detection efficiencies for electrons and ions are well below 100%, there are false coincidences where a ion is detected with an electron from a different ionization event. The probability for true coincidences and false coincidences and consequently the rate of true-to-false-coincidences can be calculated when the detection efficiencies are known, see ref. [19]. and fig.2.19.

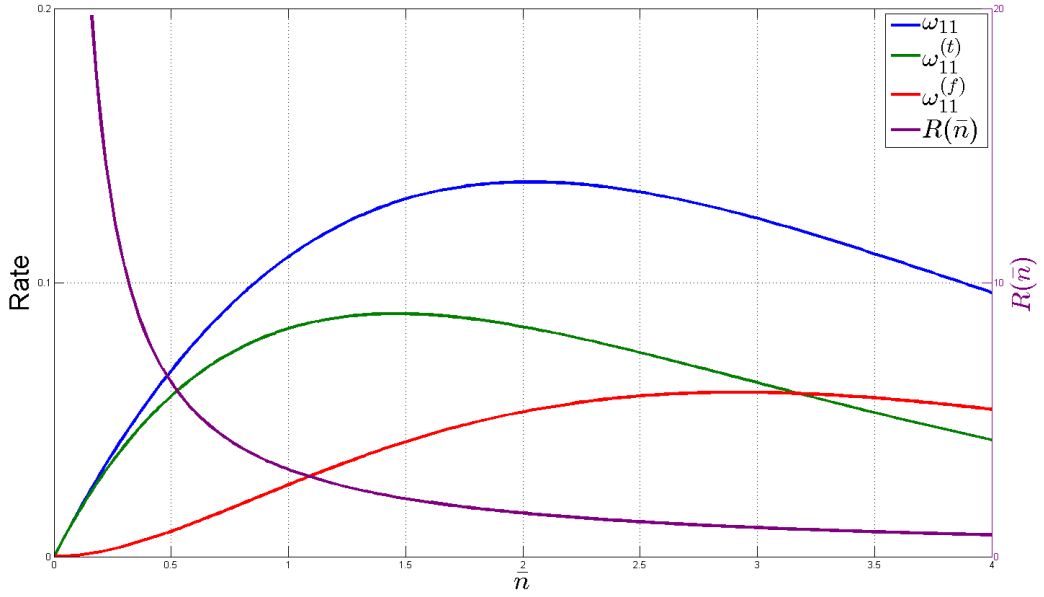

Figure 2.19: True $\omega_{11}^{(t)}$, false $\omega_{11}^{(f)}$ and total ω_{11} coincidence rates as a function of the mean ionization events per laser pulse. R indicates the ratio of true- to false coincidences. The detection efficiencies have been set to typical values of the experiments: ξ_i=0.30; ξ_e=0.55. See ref. [12]

When spectra obtained with different settings are subtracted from each other, there is not only a difference in the true-to-false ratio which causes an error but also a difference in the the rate of true coincidences. Typical mean ionization events for pump-probe experiments are in the range of 0.03 up to 0.5 $\frac{\text{events}}{\text{pulse}}$ for coincidence analysis. In this range a higher ñ results in a higher ω_{11}^{t} which consists of the coincidences coming from the pure pump-probe signal but also from the pump only and probe only signal. At this point it is

not clear whether the number of coincidences resulting from pump and probe only stays constant when ñ becomes higher. It is assumed that for low ñ <0.03 (approximately until $\omega_{11}^{(t)}$ can be linearly approximated) the subtraction is reasonable. Another important point is that the influence of the only spectra is probably overestimated. ω_{11}^{t} from pump-probe is higher than the sum of ω_{11}^{t} from pump only and probe only, the difference must be due to the pure pp-signal whereas the only parts in ω_{11}^{t} are not likely to rise but will rather tend to drop. Therefore, the probability to identify only signals as pump-probe signal is low, there is rather a chance to subtract more of the pump-probe spectrum than necessary.

Further research should be conducted on this topic as this is a delicate step in the data analysis and an intrinsic problem when pump-probe signals are acquired. Therefore an error estimation is of great interest for the whole community.

CHAPTER 3

Results on Acetone

The following sections 3.1 and 3.3.1 were published in the Journal of Physical Chemistry A with the title "Disentangling Multi-Channel Photodissociation Dynamics in Acetone by Time-Resolved Photoelectron-Photoion Coincidence Spectroscopy". Additional remarks are added in the course of this thesis in order to give more detailed explanations. The experiments were performed as part of the master's theses of Markus Bainschab and Paul Maierhofer under supervision and participation in the experiment of Ass.-Prof. Dr. Markus Koch. The main work within the author's master's thesis is the design, construction and characterization of the optical setup as described in chapter 2. Univ.-Prof. Dr. Wolfgang E. Ernst contributed to the work with his profound knowledge in molecular physics. Pascal Heim and Bernhard Thaler participated in the experiments.

3.1 Introduction

Acetone is an organic compound with the formula $(CH_3)_2CO$ (see fig.3.1) and is the simplest ketone.
With an IP of 9.7 eV it can be ionized by multi-photon-ionization with regard to the current experimental setup. As the S_1 state at 4.4 eV [20] which is resonant with 266 nm pulses is

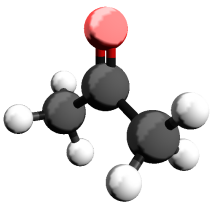

Figure 3.1: Structure of acetone. (black: carbon atoms, red: oxygen, white hydrogen)

longlived (>100 ps) [21] and leads to Norrish Type I dissociation, acetone is a proper candidate for our experimental setup.

Photodissociation of acetone is one of the most comprehensively studied photochemical reactions [22]. Acetone is a prototype molecule for the so-called Norrish type I (NT1) reaction in ketones and aldehydes, where CC bond cleavage is induced by photoexcitation and leads, in the case of acetone, to dissociation to acetyl and methyl radicals. Aiming at a mechanistic picture of the NT1 reaction in acetone, excitation dynamics are extensively studied in gas-phase with time-resolved mass spectrometry (TRMS) and time-resolved photoelectron spectroscopy (TRPES) for excitation to S_1 [23, 24], S_2 [25–30] and S_n Rydberg states [20, 31, 32]. The interpretation of ion and electron transients turns out to be difficult because multiple pump-probe ionization channels are active [20]. The reasons are a very low S_0-S_1 excitation cross section [33], requiring high laser intensities and resulting in a high probability for two-photon excitation, and ultrafast geometry relaxation of the S_1 population in combination with S_3 excitation by a second pump photon [20,21]. TRMS and TRPES spectra are therefore influenced by a combination of dynamics in various excited states and contributions of different channels to the same ion fragment cannot be distinguished with these methods.

For investigation of photodissociation reactions the ability to distinguish whether dissociation occurs actually in the neutral, excited molecule or is rather induced by the probe pulse and happens after ionization, is essential and not deducible from TRMS experiments. For example, one- and two photon excitation experiments to Rydberg states at 8-9 eV energy lead to different conclusions about the underlying dynamics. The two-photon ion transients show sub-ps dynamics only in the acetyl ion fragment signal, leading to the interpretation that a NT1 dissociation is active on the S_2 surface of the neutral molecule [32]. One-photon excitation, in contrast, leads to the same sub-picosecond decay in both parent and fragment transients, which is interpreted as ionization of undissociated molecules and fragmentation of the ion [31].

We apply time-resolved photoelectron-photoion coincidence (PEPICO) detection, a highly selective probe technique [11, 34–36], to disentangle the fragmentation and relaxation behavior of the different ionization channels. The coincidence detection for each ionization event allows assignment to an ionization channel based on the electron kinetic energy and the correspondingly detected ion provides information about fragmentation in this channel. For more detail about the experimental setup see chapter 2.

3.2 Single Pulse Results

Before time-resolved experiments were conducted, the spectra of pump- and probe only were acquired for 800 nm, 400 nm and 266 nm pulses. See results in the following figures 3.2, 3.3 and 3.4. For a detailed discussion of the spectra and possible transition and ionization states see [12]. At this point the spectra are needed for comparison to time-resolved results.

800 nm

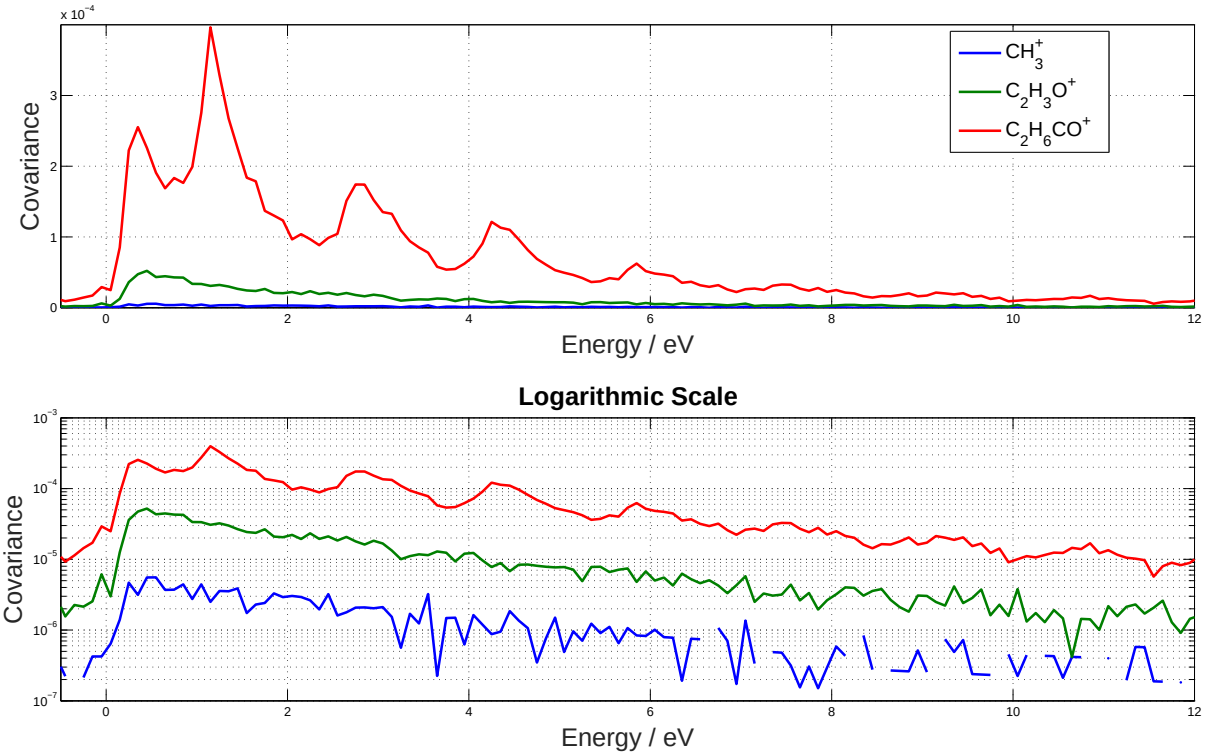

Figure 3.2: Acetone 800 nm PEPICO spectrum, 80 mW laser power, pressure $5 \cdot 10^{-6}$ mbar, eiTOF_262-266

In fig.3.2 the 800 nm PEPICO spectrum of acetone is shown. The main component of the signal results from the parent which also shows a clear ATI peak structure, the peaks are separated by the photon energy of 1.55 eV. The acetyl fragment does not show this structure, most probably because there are a lot of possible ionization states which smears out the structure. There is hardly any signal from the methyl fragment which indicates a low probability for both ionization of the neutral methyl fragment and a low probability

for the generation of a charged methyl ion upon ionization and subsequent fragmentation of the parent molecule.

400 nm

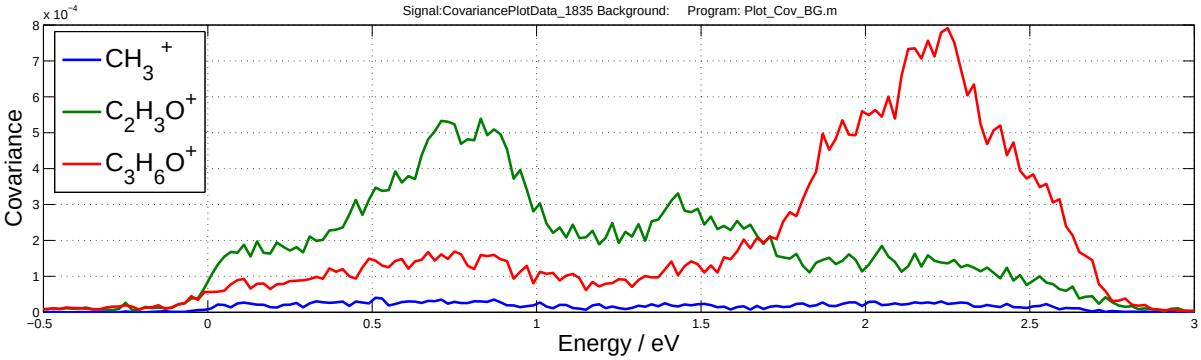

Figure 3.3: Acetone 400 nm PEPICO spectrum, 40 mW laser power, pressure $5 \cdot 10^{-6}$ mbar.

Fig. 3.3 shows the PEPICO spectrum of acetone ionized with 400 nm pulses. There is both a strong peak from the parent and the acetyl fragment and again hardly any signal from the methyl fragment. The fragment spectrum is centred at about 0.7 eV with a second peak at approximately 1.4 eV. There is an underlying parent signal but also a strong parent signal at 2.3 eV. In general there is more fragment signal at lower energies and more parent signal at higher electron energies. As there is more energy converted in vibrational energy -which lowers the kinetic energies of the released electrons- the molecule is more likely to fragment.

266 nm

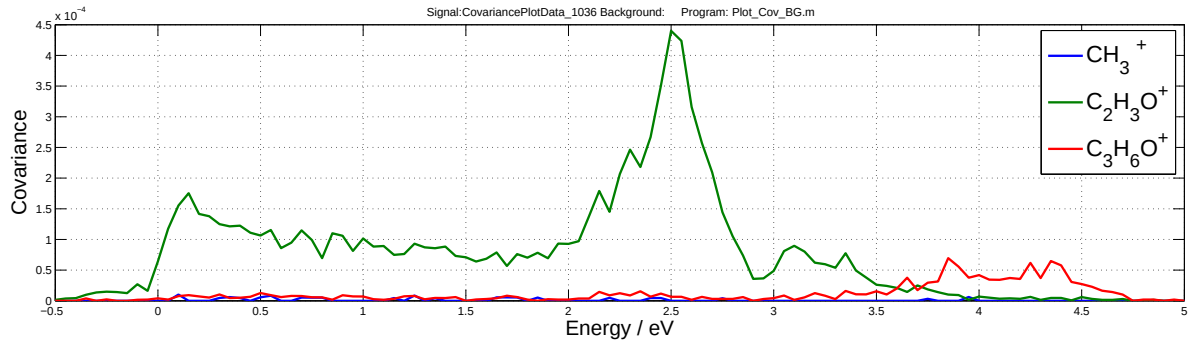

Figure 3.4: Acetone 266 nm PEPICO spectrum, 13 mW laser power, pressure $5 \cdot 10^{-6}$ mbar.

Fig.3.4 shows the PEPICO spectrum of acetone ionized with 266 nm only. Again there is hardly any signal from the methyl fragment which again highlights the low probability for a fragmentation leading to a charged methyl fragment.
There is a broad acetyl structure from 0 eV to almost 4 eV which results mostly from background electrons. The signal has peaks at 0.1 eV and 2.5 eV. The parent signal is almost zero in this region and has its onset at 3.5 eV. The structure expands up to 4.7 eV and has no clear peak. Again the fragment electron energies are lower than the observed parent energies.

3.3 Time-Resolved Pump-Probe Results

3.3.1 269 nm pump 405 nm probe

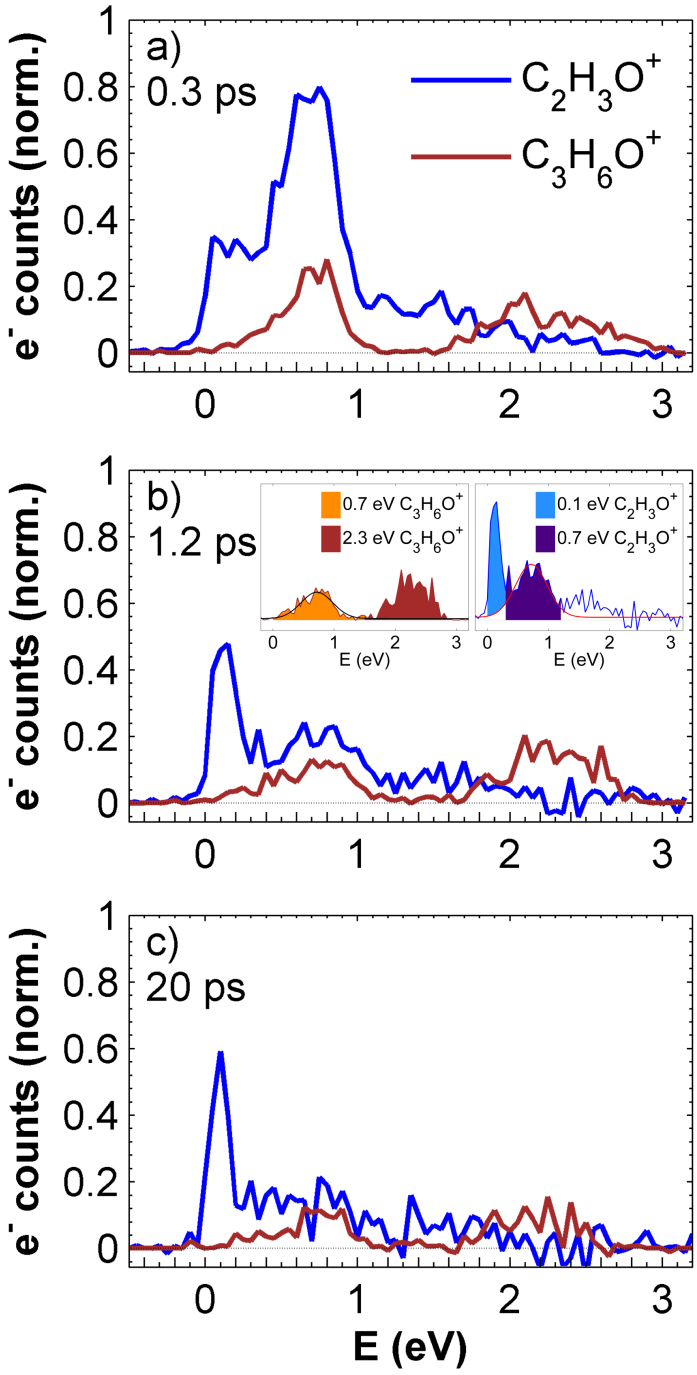

Figure 3.5: Temporal evolution of the pump (4.6 eV) - probe (3.1 eV) PEPICO signals associated with the acetone parent ion ($C_3H_6O^+$, 58 u, red curve) and the acetyl fragment ion ($C_2H_3O^+$, 43 u, blue curve), for pump-probe time delays of 0.3 (a), 1.2 (b) and 20 ps (c). The inset in b) shows the energy range over which the PEPICO signals are integrated for the parent (left) and fragment (right), to determine time- and power dependencies (depicted in fig.3.8).

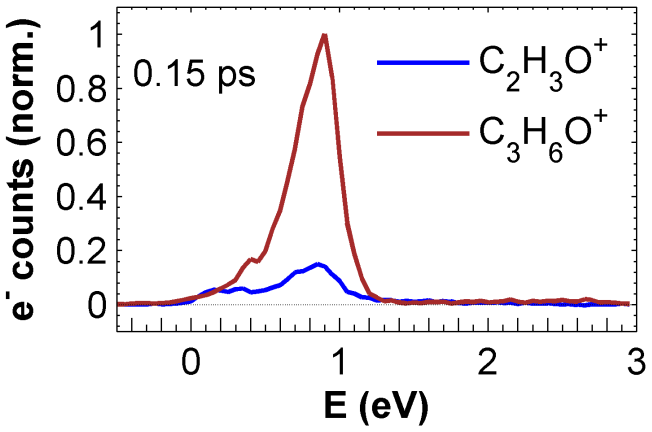

Figure 3.6: PEPICO spectrum in the pump-probe temporal overlap region at a delay of 0.15 ps. The acetone parent ions (red) strongly dominate over the acetyl fragment ions (blue) due to an additional ionization channel that requires the simultaneous presence of pump and probe photons. Note that this photoelectron band appears at higher energies (0.9 eV maximum) than the S_3 band (0.7 eV).

Fig. 3.5 shows PEPICO spectra associated with the acetone parent ion ($C_3H_6O^+$, 58 u, red curve) and the acetyl fragment ion ($C_2H_3O^+$, 43 u, blue curve) for three different pump-probe time delays of 0.3 (a), 1.2 (b) and 20 ps (c). The spectra show three prominent photoelectron (PE) bands centered at 0.1, 0.7 and 2.3 eV. The 0.1 eV band is detected only in coincidence with the fragment, the 0.7 eV band in coincidence with both fragment and parent, and the 2.3 eV band only in coincidence with the parent ion. The 0.1 V band remains constant within the time window of the experiment (20 ps, Fig. 3.5 1c), while the 0.7 and 2.3 eV bands both decrease. For pump-probe delays below 300 fs an additional ionization channel becomes active due to the temporal overlap of the pump and probe pulse. In this channel unfragmented parent ions are efficiently produced, as shown in fig.3.6.

The two PE bands at 0.7 and 2.3 eV (fig. 3.5) can be assigned to ionization from different Rydberg states and thus to ionization channels proceeding via these states, based on experimental and calculated excited state energies, as shown in fig.3.7. Two pump photons (E_{pu} = 4.6 eV) excite the molecule resonantly via S_1 to high-lying Rydberg states. With a total excitation energy of 9.2 eV and the given spectral width, the 6s, 6p, 5d and 6d states can be reached [33], for which the collective term S_n is used.

The PE band centered at 2.3 eV and observed in the parent PEPICO signal in fig.3.5 can be explained by ionization with one probe photon (E_{pr} = 3.1 eV) from the S_n states that are populated. The upper limit of the electron kinetic energy obtained with this process is $2E_{pu} + E_{pr}$ - 9.7 eV = 2.6 eV. Note that electron kinetic energies above this limit can occur due to the spectral width of the laser pulses. Because several Rydberg states (6s,

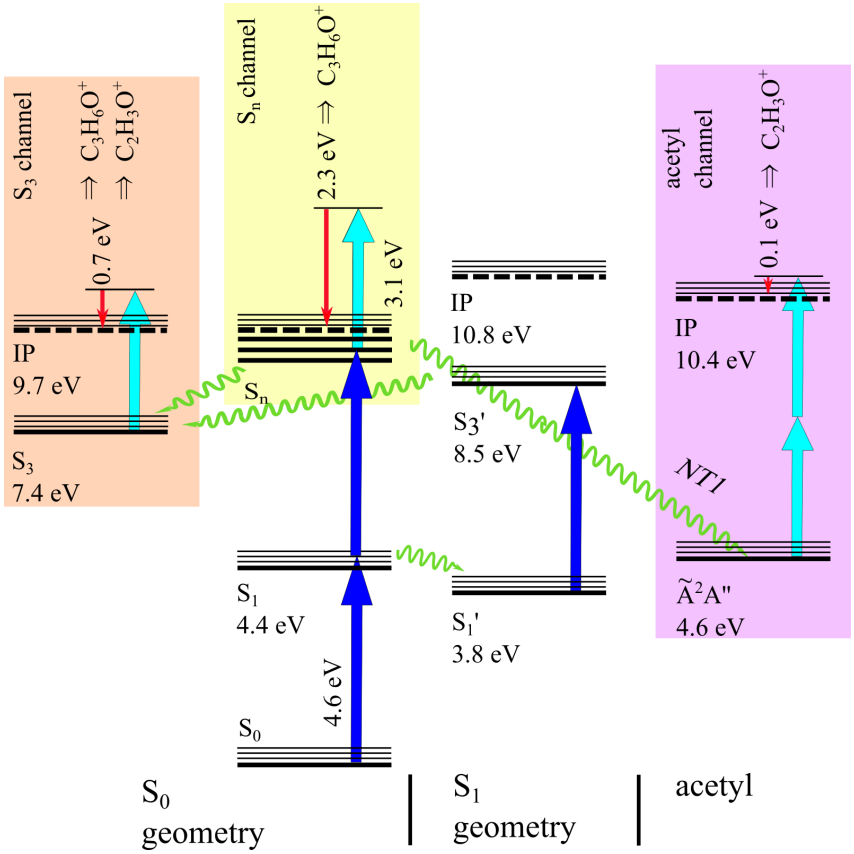

Figure 3.7: Energy diagram for acetone with relevant levels in the ground state geometry (left) [33, 37] and S_1 geometry (center) [20], and for acetyl radicals (right) [32]. Energy values are relative to the acetone ground state. Shown are photoexcitations (vertical arrows, blue: 4.6 eV pump, cyan: 3.1 eV probe), photoelectrons (red, downward pointing arrows) with corresponding energies, and relaxation pathways (green, wavy arrows).

6p, 5d and 6d) lie within the excitation bandwidth, this PE band is broader than the other bands.

The 0.7 eV band, as observed in the parent and fragment PEPICO signal, corresponds to ionization with one probe photon from the S_3 state (fig.3.7). With an IP of 2.3 eV relative to the S_3 state, the expected PE energy is E_{pr} -2.3 = 0.8 eV, which fits almost perfectly the observed value of 0.7 eV. As proposed by Rusteika et al. [20], the S_3 state can be populated by direct two pump photon excitation to S_n Rydberg states followed by internal conversion to S_3 through crossings with valence states (fig.3.7) [38]. Alternatively, it can be populated by a sequential process consisting of a one-photon excitation to S_1 combined with ultrafast geometry relaxation [21] and S_3' excitation by a second pump photon in the S_1 geometry. Note that in both pathways approximately 1.8 eV vibrational energy ($2E_{pu}$ – 7.4 eV = 1.8 eV) is deposited in the ion. The 0.1 eV band is observed exclusively in coincidence with the fragment ion, indicating that it is correlated to ionization of neutral acetyl molecules (fig.3.7). The electron kinetic energy suggests a two probe-photon ionization of the excited acetyl radical in the Ã2A" state, which has a calculated IP of 5.8 eV ($2E_{pr}$ - 5.8 eV = 0.3 eV) [32]. The 0.1 eV band has its onset at almost 0 eV and appears to be narrower compared to the other bands. This could be because only part of the acetyl

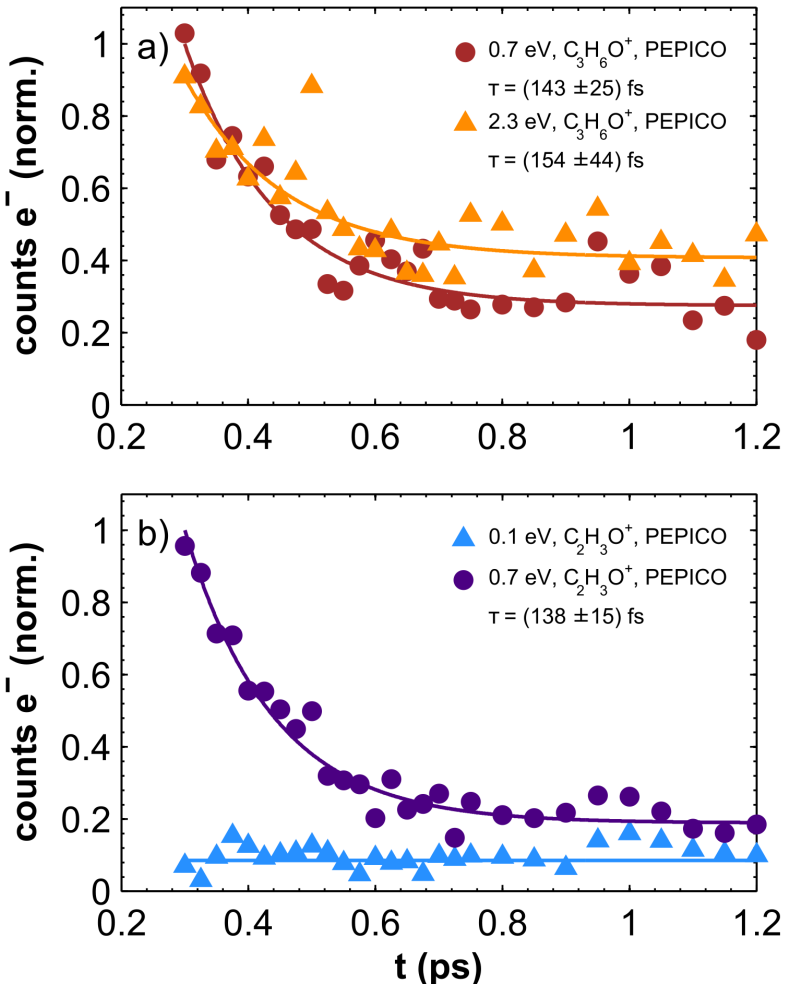

Figure 3.8: Transient change of the 0.7 eV (red) and 2.3 eV (orange) parent PEPICO signals (a), as well as the 0.1 eV (blue) and 0.7 eV (purple) fragment PEPICO signals (b). Lines represent single exponential decays, with the time constants τ shown in the legend.

population is in the energetic detection window of the probe laser, or because of similar geometries of the Ã2A" and the ionic state, in other words, a smaller Franck-Condon window.

To learn about the photoinduced relaxation dynamics of each of the three channels we monitor the transient change of the PEPICO signals up to 1.2 ps pump-probe delay. Therefore, corresponding energy regions in the PEPICO spectra, as indicated by shaded areas in the inset of fig.3.5b, are integrated in the following way:
We determine changes of the PEPICO signal by integrating energetic regions in the PEPICO spectra, as shown in fig.3.9. While in the parent signal the 0.7 and 2.1 eV bands are well separated (a), the fragment bands at 0.1 eV and 0.7 eV overlap (b). We separate these two fragment contributions by assuming that the 0.7 eV parent and fragment PEPICO signals have the same lineshape as we assume that they have the same origin. We fit the 0.7 eV parent signal with the sum of two Gaussians eq.3.1 (fig3.9a) and scale the fit result to the 0.7 eV fragment signal (fig.3.9b). The 0.1 eV peak area is then

determined as signal area above the Gaussian function, as indicated by the blue area in fig.3.9b.

$$signal(E) = a_1 e^{-(E-a_2)/a_3} + b_1 e^{-(E-b_2)/b_3} \tag{3.1}$$

Where $signal(E)$ is the signal as a function of the electron energy E in eV, a_n and b_n are the fit parameters. There is no physical meaning in the fit function, it was chosen because it describes the lineshape good enough in order to separate the fragment contributions. The fit parameters are listed in the following table 3.1. The amplitude of the fit function was scaled to fit the amplitude of the 0.7 eV peak of the fragment in fig.3.9b.

Table 3.1: Fitparameters from equation 3.1 to the 0.7 eV parent signal in fig.3.9.

parameter	**value**
a_1	(9.7 ± 1.1) a.u.
a_2	(0.6 ± 0.1) eV
a_3	(0.36 ± 0.07) eV
b_1	(10 ± 2) a.u.
b_2	(0.87 ± 0.02) eV
b_3	(0.16 ± 0.05) eV

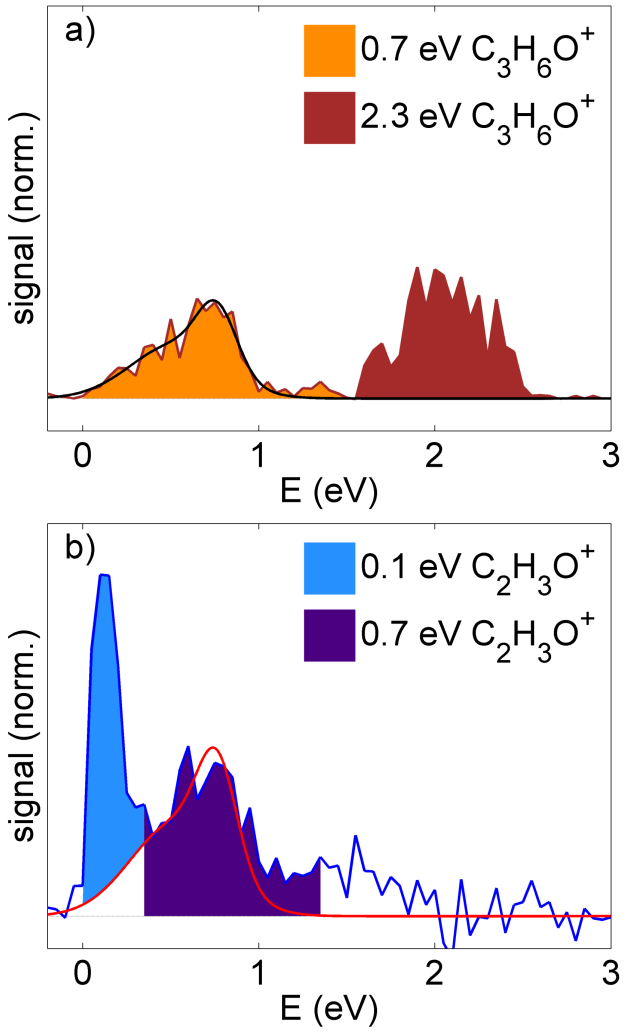

Figure 3.9: Parent (a) and fragment (b) PEPICO spectra at 1.2 ps pump-probe delay. The shaded areas indicate the energetic regions over which the PEPICO signal is integrated. A Gaussian Fit to the 0.7 eV parent and fragment band is used to separate the overlapping fragment signals.

Figure 3.8 shows the pump-probe delay dependencies of the 0.7 eV and 2.3 eV parent PEPICO signals (a) and of the 0.1 eV and 0.7 eV acetyl fragment ion PEPICO signals (b). The decaying signals in fig.3.8 were fitted with a single exponential decay and corresponding time constants τ are shown in the figure legend. The 0.7 and 2.3 eV bands decay with nearly the same time constant of, on average, (147 ± 28) fs, while the 0.1 eV fragment PEPICO signal is constant. The similarity in the S_n and S_3 decay times is not surprising as these Rydberg states have similar geometries and are close in energy [38]. The decay times observed here with 9.2 eV excitation energy are in line with previous results of 420 fs (8.1 eV excitation) [32] and 250 fs (8.78 eV excitation) [20], confirming a trend of shorter

lifetimes for higher excitation energies. The 0.7 eV parent and fragment PEPICO signals exhibit a very similar signal decrease to 20% of the initial 0.3 ps value while the 2.3 eV parent PEPICO signal shows a weaker decrease to ≈ 45%. All channels show a persistent signal that remains constant at least up to 20 ps (fig.3.5). The parent-to-fragment ratio of the 0.7 eV PEPICO band has a constant value of (37 ± 3)% within the observed time window, as determined from the ratio of the corresponding fit functions.

The number of pump photons required for excitation in each ionization channel is obtained from pump-pulse energy dependencies of the PEPICO signals, see fig.3.10. In a log-log plot we obtain linear dependencies of all PEPICO signals with slopes between 1.2 and 1.7. We conclude that all observed ionization channels are associated with the absorption of two pump photons [2, 39]. We assume that the laser intensities are not high enough to saturate the signal meaning that all molecules are ionized in the region of the highest intensity of the pulse which would lower the slope significantly. [2].
Furthermore, the fragment-to-parent ratio of the S_3 channel does not depend on the pump power. At 20 ps pump-probe delay, the persistent 0.1 eV component shows the same power dependence as at 0.5 ps.

3.3.1.1 Discussion

We begin the discussion of our PEPICO results with the S_3 channel. The 0.7 eV PE band appears in coincidence with both parent acetone ions and acetyl fragment ions (fig.3.5). Both PEPICO signals result from the same pump-probe channel because of the following four reasons: a) The PE bands have the same energy and shape (fig.3.5), b) both decay with the same decay time constant (fig.3.8), c) both show a similar relative decrease in intensity during this decay, and d) both are two-pump-photon processes. The parent PEPICO signal proves that unfragmented acetone molecules are ionized. Fragmentation in the S_3 channel occurs after ionization and is caused by relaxation mechanisms that transfer population from the initially excited S_n Rydberg states to the S_3 Rydberg state. This relaxation is facilitated by crossings with valence states [38] and 1.8 eV of electronic energy are converted to vibrational energy. In principle, fragmentation could also be caused by resonant absorption of further probe photons by the unfragmented parent ion after ionization [34]. We exclude this option because fragmentation should then also occur in the 2.3 eV S_n channel, which is not the case (fig3.5). The energy conversion process has to be completed within the first 300 fs because the fragment-to-parent ratio is constant

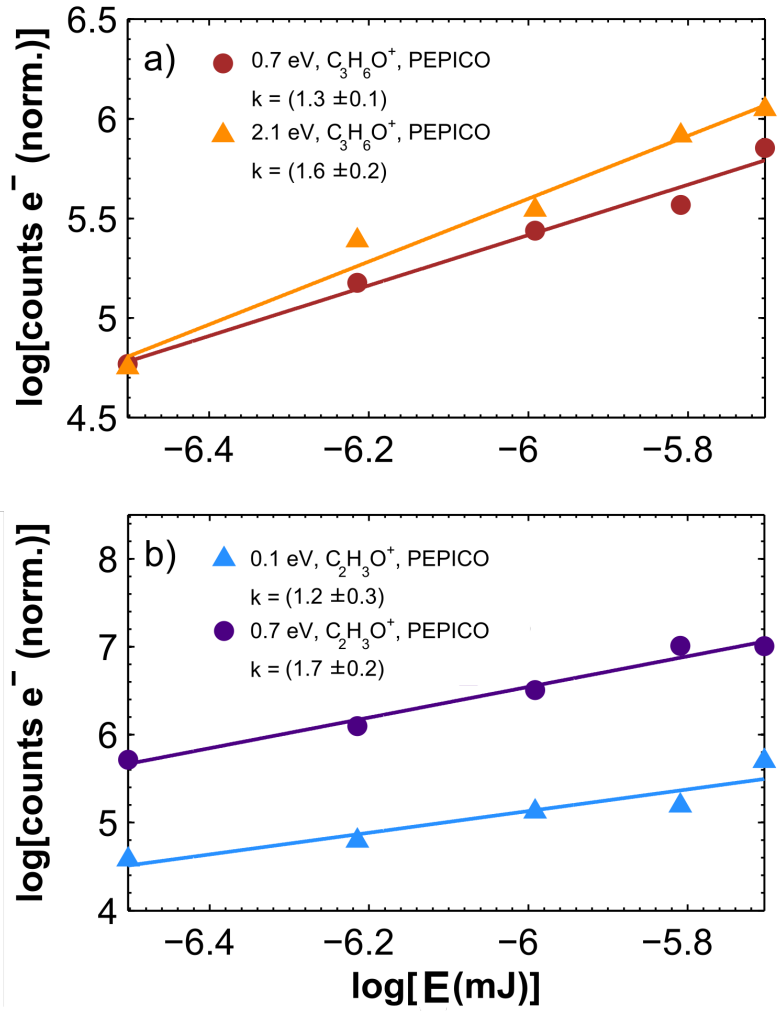

Figure 3.10: Pump-pulse energy dependencies of the parent (a) and fragment (b) PEPICO signals at 0.5 ps time delay. PEPICO signals are obtained by integrating over the energetic regions shown in fig.3.9. The pulse energy was varied from 1.5 to 3.3 μJ. The slopes of linear fits in the log-log plot are shown in the legend.

above this pump-probe delay. We note that in synchrotron experiments almost complete fragmentation is observed at an excess energy of 0.9 eV [13], although for an ionization pathway including an autoionizing state, which is different from the pump-probe path of our experiment. The fact that (37 ± 3)% of the parent ions remain intact despite 1.8 eV of vibrational energy deposited in the molecule, demonstrates that intramolecular vibrational energy redistribution is very efficient so that vibrational energy is stored in modes that do not couple efficiently to the CC-stretch, the reaction coordinate responsible for CH_3 separation.

The Sn channel does not lead to fragmentation because the 2.3 eV PEPICO band is observed only in coincidence with parent ions. This is reasonable as direct population of S_n Rydberg states by two pump photons does not involve energy conversion to vibrations because the geometry of the S_0 ground state is similar to that of the S_n Rydberg states [38]. While the S_3 and S_n channels and their time evolutions are in agreement with previous

TRPES results [20] a clear and quantitative assignment of the fragmentation behavior in both channels is only possible with our coincidence measurements. Both channels contribute to unfragmented parent ions (fig.3.5) which cannot be distinguished with less-selective probe techniques. Furthermore, in spite of originating from different excited states, both channels decay with the same time constant, a fact that typically leads to the interpretation of the same underlying process [20, 31]. Our results thus demonstrate the danger of misinterpretation with less-selective techniques if multiple channels are present. The PEPICO spectra also unequivocally show that during the observed sub-ps dynamics, fragmentation in the S_3 channel does not occur in the neutral molecule. Previous TRMS experiments, in contrast, were interpreted in terms of a fast (≈100 fs) NT1 dissociation in the neutral, excited molecule, followed by a further sub-ps decay [32] because the corresponding sub-ps transient was observed only in the fragment ion and not in the parent ion signal. Our PEPICO results show that during the pump-probe temporal overlap an ionization channel becomes active that efficiently produces parent ions due to the simultaneous presence of 4.6 eV and 3.1 eV photons (see fig.3.6). This strong parent signal easily overshadows the much weaker sub-ps decay of the parent. In a recent TRMS study the sub-ps parent decay was observed very weakly (≈3%)10 [20] and with one-photon 8.0 eV excitation it is clearly observed because ≈4.6 eV photons are not present [31]. Both results support our interpretation.

The persistent signals in the S_3 and S_n channel and the corresponding difference in the relative signal decays of the two channels (fig.3.8), underline that the relaxation pathways are different. The Rydberg states are crossed by valence states which provide efficient relaxation pathways [38] and the persistent signals represent the fractions of populations that are below the barrier for internal conversion, which are different for the S_3 and S_n states. The reason for the sub-ps decay might be relaxation to states that are outside the detection window, similar to a proposed mechanism in the S_1 state [21], probably including dissociation, as has been suggested as the main decay channel for high-lying Rydberg states [32]. The non-decaying character of the 0.1 eV acetyl fragment PEPICO band is a clear difference to the temporal behavior of the S_n and S_3 channels (fig.3.5 & 3.8). The complete absence of parent ions (fig.3.5) suggests that it results from ionization of neutral acetyl radicals that originate from NT1 dissociation, which is supported by the energy of the band. This is in line with a previous experiment where a persistent fragment ion component was interpreted as signature for a NT1 reaction [31]. Calculations [32] predict a relaxation pathway leading from highly excited Rydberg states to the S_2 state,

where the NT1 dissociation occurs. Further sub-ps relaxation populates the acetyl $\tilde{A}2A''$ state, which we propose to be responsible for the 0.1 eV band. This path thus delivers an explanation for the 0.1 eV fragment PEPICO signal, provided that the acetyl $\tilde{A}2A''$ excited state is populated within 300 fs and that it is long lived (100 ps). We note that the 0.1 eV PEPICO band cannot be connected to the S_1 state because it is correlated with a two-pump-photon process.

In combination, the observation of the three distinct channels (S_n, S_3 and acetyl) suggests that after excitation of the S_n Rydberg states the wavepacket splits. Certain fractions lead to ultrafast population of the S_3 state and through NT1 dissociation to acetyl radicals, both on time scales well below 300 fs. The fact that neutral acetyl radicals require two probe photons for ionization while the S_3 and S_n states require only one, in combination with roughly equal strengths of the corresponding PEPICO signals, indicates that a majority of the trajectories follow the acetyl pathway. While the excited acetyl radical is long lived (20 ps) the remaining S_n population and the S_3 population undergo sub-ps decays. The fragmentation behavior and time evolution of the three channels could only be disentangled completely due to the high selectivity of PEPICO probing. It is anticipated that PEPICO detection is essential if multiple excitation pathways are to be expected, such as in the field of two-photon absorption and their applications.

3.3.1.2 Search for Methyl Radical

As the Norrish Type-1 reaction takes place methyl and acetyl radicals are formed. These fragments are neutral and can be ionized subsequently. Surprisingly hardly any signal from an ionized methyl radical was found within our experiments. If the ionization probability of the neutral methyl radical ($I_P = 9.84$ eV) is higher than the probability for the formation of an ionized methyl fragment by ionization and fragmentation of an acetone molecule, a rise of the methyl-ion signal should occur for increasing delays. This rise could not be observed using a variety of 266 nm pump and 400 nm probe intensities. Possible reasons are:

- the ionization probabilities do not behave as described above
- pump and probe powers that are mandatory for monitoring this effect are not accessible within the limits of the setup
- the pump wavelength is short enough to overcome the barrier for fragmentation due

to vibronic excitations and no ISC is needed. The fragmentation takes place faster in this case and cannot be resolved.

3.3.2 266 nm pump 800 nm probe

266 nm pump 800 nm probe experiments on acetone were conducted. The results are preliminary and are an initiation for further research on acetone using 800 nm probe pulses.

Fig. 3.11 shows a 266 nm pump 800 nm probe PEPICO spectrum of acetone at a time delay of 150 fs.

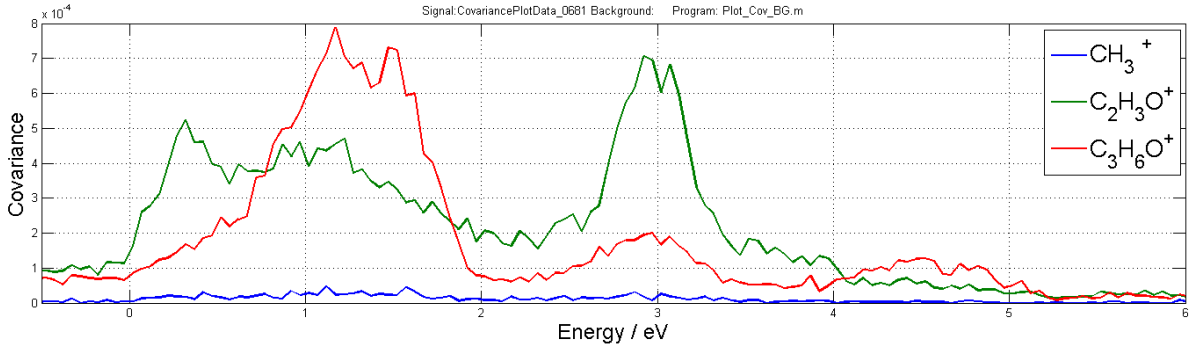

Figure 3.11: PEPICO spectrum 266 nm, 23 mW pump; 800 nm, 15 mW probe; 150 fs timedelay, $5 \cdot 10^{-6}$ mbar acetone

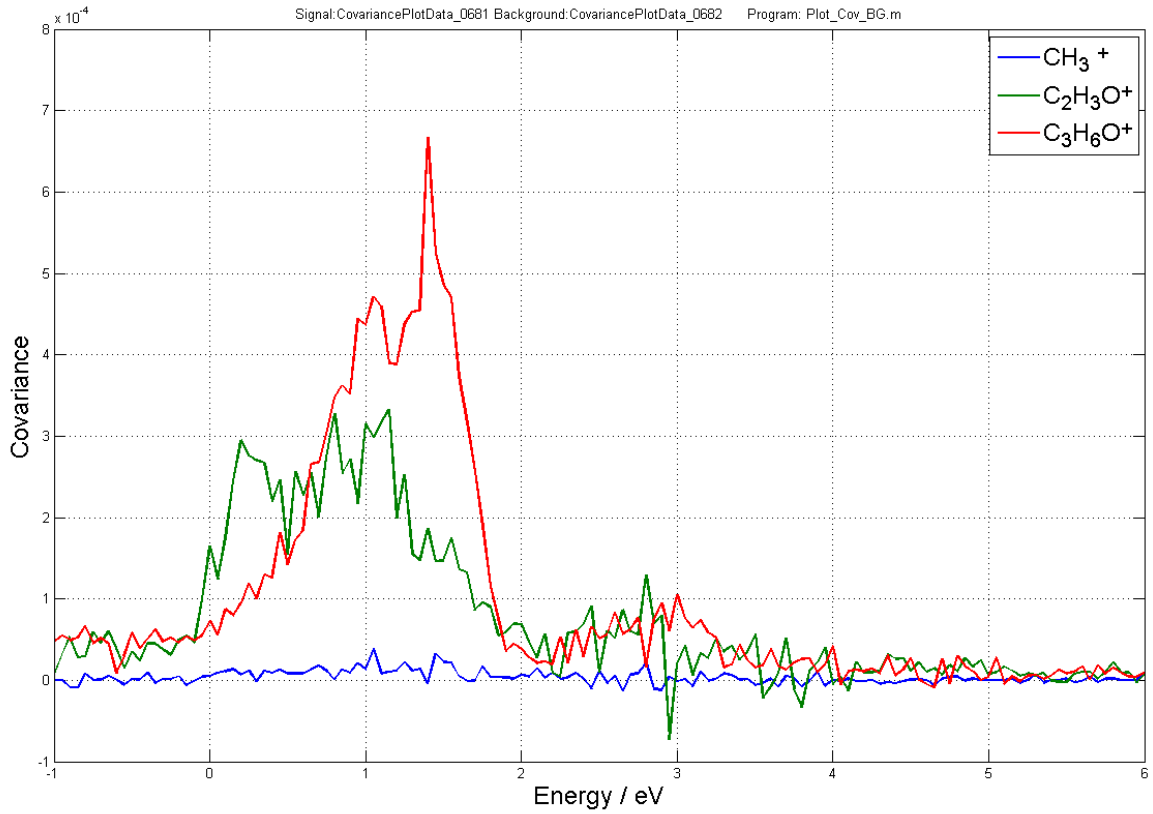

Figure 3.12: PEPICO difference spectrum 266 nm, 23 mW pump; 800 nm, 15 mW probe; 150 fs timedelay (eiTOF_681) minus probe-pump 3 ps timedelay (eiTOF_682), $5 \cdot 10^{-6}$ mbar acetone

Fig.3.12 shows the same spectrum as fig.3.11 but with subtracted probe-pump spectrum. As the 800 nm probe supposingly does not pump any population the subtraction seems reasonable in order to get the pump-probe signal. There are issues with the subtraction of signals in general, see sec.2.2.1 The spectrum shows hardly any methyl signal. The structure at around 2.9 eV seems not to origin from the pump-probe signal as the remaining signal is not significantly higher than the noise level. Further investigation is necessary. The acetyl fragment has a broad structure between 0 eV and about 2 eV and peaks at approximately 0.2 eV, 0.8 eV and 1.1 eV. The parent structure has its onset at 0 eV, peaks at 1 and 1.4 eV and goes rapidly down to zero at 1.9 eV. For some peaks possible transition states were found. See fig.3.13 for the energy level diagram of acetone.

The 1 eV peak most likely results from a two photon excitation to S_n and a one photon ionization. The reason that both parent and fragment signal is detected at 1 eV can either be that the fragment signal originates from an other channel or that this direct channel

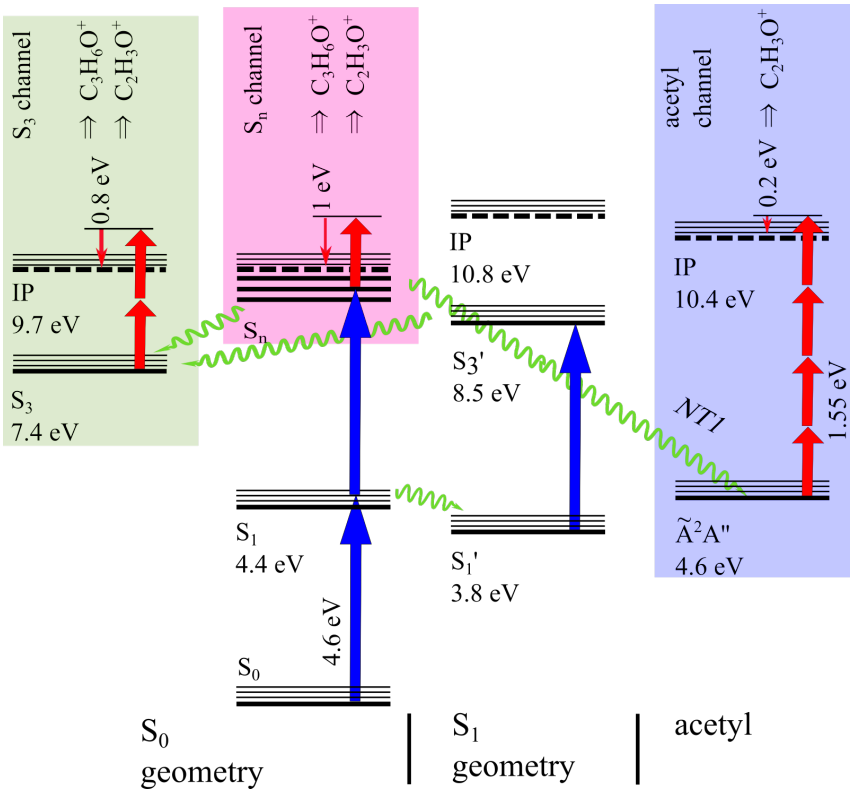

Figure 3.13: Energy diagram for acetone with relevant levels in the ground state geometry (left) [33, 37] and S_1 geometry (center) [20], and for acetyl radicals (right) [32]. Energy values are relative to the acetone ground state. Shown are photoexcitations (vertical arrows, blue: 4.6 eV pump, red: 1.55 eV probe), photoelectrons (red, downward pointing arrows) with corresponding energies, and relaxation pathways (green, wavy arrows).

can also lead to fragmentation which is not in line with the results from sec.3.3.1. The fragment peak at 0.2 eV can be caused by two photon excitation to an S_n state where Norrish-type 1 dissociation takes place. The acetyl fragment is then ionized by 6 probe photons leading to an electron energy of 0.2 eV. This is supported by the fact that the parent signal shows no peak at 0.2 eV energy. The structure at around 0.8 eV is likely to be caused by two photon excitation to S_n and relaxation S_3 with two photon ionization. The prominent 1.4 eV peak from the parent signal could not be connected to a ionization channel.

In principle the same ionization channels as observed with 400 nm probe are observed which is not surprising as the only main difference in the two experiments is that the 400 nm probe photons have twice the energy of the 800 nm photons which only shifts the spectra. The dynamics in the molecules are triggered by the pump photons which are the same for both setups. Further research is recommended.

Also the ion yield was measured as a function of the time delay between pump and probe. See fig.3.14. The most interesting feature can be seen at 0 fs time delay where the parent signal peaks while the acetyl fragment yield dips. As there is no time for relaxation, the molecule can not gain vibrational energy which would cause fragmentation. Once the overlap in time is lost, the ion yield of acetyl goes back to the level of probe-pump

case while the parent ion yield falls down rather slow indicating a long living transition state which does not promote fragmentation after ionization. The S_n states are possible transition states.

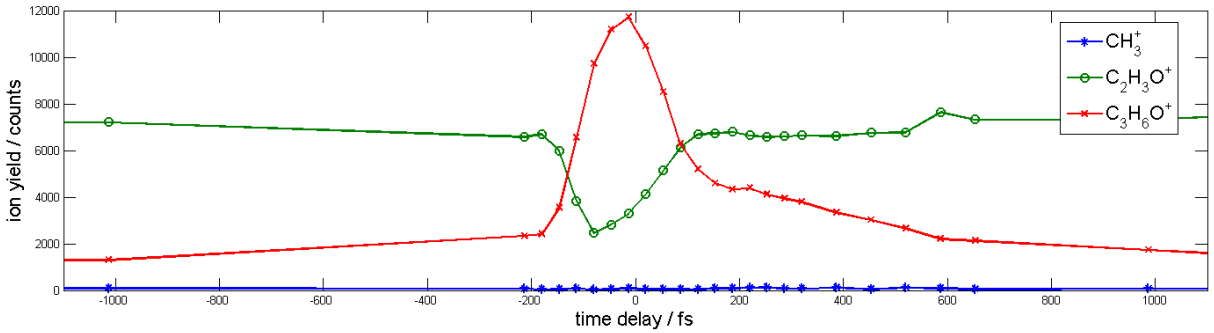

Figure 3.14: Ion yield over time delay; 266 nm, 22 mW pump; 800 nm, 15 mW probe; $5 \cdot 10^{-6}$ mbar acetone, eiTOF_0727-0752.

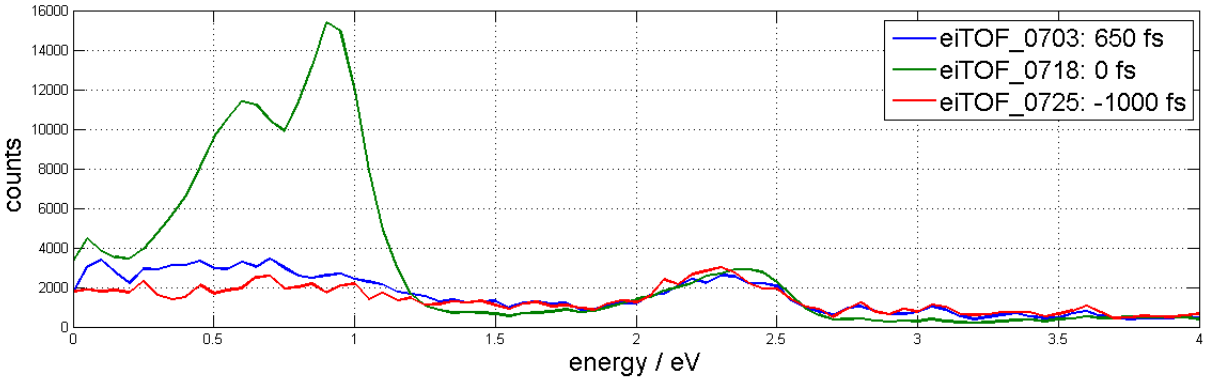

Figure 3.15: Integrated electron energy spectra at different time delays.

Fig.3.15 shows integrated electron energy spectra at three different time delays. Beginning from 1.2 eV the spectra overlap and do not show a significant time delay dependence and therefore can be associated with pump and probe only spectra which is in line with fig.3.12 where the pump-probe minus the probe-pump spectrum is shown. The time dependent signal occurs between 0 eV and 1.2 eV. Fig.3.16 shows the integrated electron yield of interesting peaks as a function of time delay. For positive time delays there is clearly some dynamic triggered by the pump as the asymmetric signal indicates. The PE band centered at around 0.7 eV seems to decay slower than the 1 eV PE band.

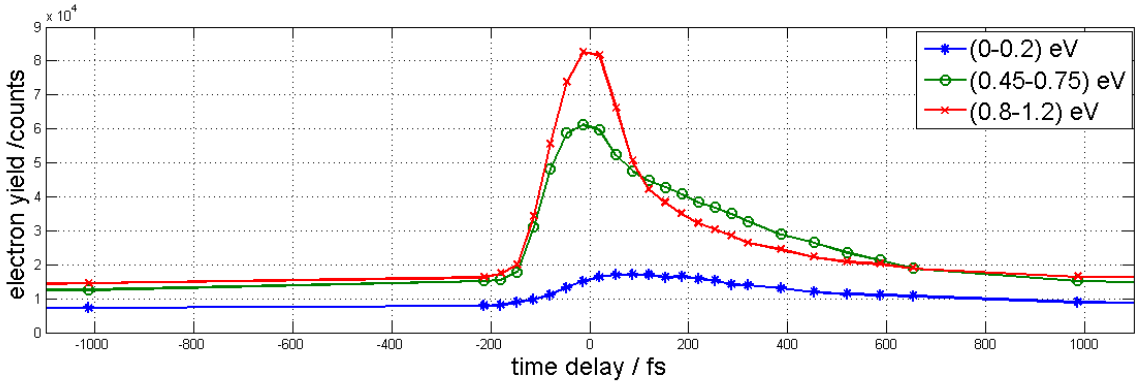

Figure 3.16: Electron yield over time delay for different energy windows; 266 nm, 22 mW pump; 800 nm, 15 mW probe; $5 \cdot 10^{-6}$ mbar acetone, eiTOF_0701-0726.

As the 266 nm pump, 800 nm probe results are rather preliminary, further research is recommended. For a systematic understanding of the triggered dynamics the following experiments are proposed:

- Electron energy peak resolved power scans, both for the pump and the probe power in order to identify the underlying channels. As multi-photon probing is highly likely in the case of 800 nm probe wavelength, this could be a key to understand the spectra.
- A detailed PEPICO timescan should be conducted in order to find the relaxation time-constants of the PE bands to support the interpretation.
- A detailed comparison of probe-pump spectra and pump- and probe-only spectra should be done in order to exclude the option that 800 nm pumping is possible.

3.3.3 Signal from the S_1 state

For the investigation of the Norrish-type 1 reaction, pump-probe signal from the S_1 state is of major interest but was not to be found within the experiments of this thesis. This is probably due to the relatively small cross section for the transition S_0-S_1 [33]. High intensities are needed in order to populate the S_1 state which also leads to the population of higher lying states which overshadow the S_1 signal.
The author suggests to go to such low pump powers that no signal from pump-only is acquired but to increase the probe power. This way the probability to populate higher lying states with the pump pulse gets lower while the higher probe intensities are needed in order to probe the S_1 state.

Bibliography

[1] C. E. Wayne, R. P. Wayne. *Photochemistry.* Oxford University Press, New York, 1996

[2] I. V. Hertel, C.-P. Schulz. *Atome, Moleküle und optische Physik 1.* Springer-Verlag, 2008

[3] I. V. Hertel, W. Radloff. Ultrafast dynamics in isolated molecules and molecular clusters. *Rep. Prog. Phys.* **69** (2006) 1897

[4] G. Wu, P. Hockett, A. Stolow. Time-resolved photoelectron spectroscopy: from wavepackets to observables. *Phys. Chem. Chem. Phys.* **13** (2011) 18447

[5] A. Stolow, A. E. Bragg, D. M. Neumark. Femtosecond time-resolved photoelectron spectroscopy. *Chem. Rev.* **104** (2004) 1719

[6] A. Stolow. Femtosecond time-resolved photoelectron spectroscopy of polyatomic molecules. *Annual Review of Physical Chemistry* **54** (2003) 89

[7] S. Lochbrunner, J. J. Larsen, J. P. Shaffer, M. Schmitt, T. Schultz, J. G. Underwood, A. Stolow. Methods and applications of femtosecond time-resolved photoelectron spectroscopy. *Journal of Electron Spectroscopy and Related Phenomena* **112** (2000) 183

[8] I. Fischer, M. J. Vrakking, D. Villeneuve, A. Stolow. Femtosecond time-resolved zero kinetic energy photoelectron and photoionization spectroscopy studies of I2 wavepacket dynamics. *Chemical Physics* **207** (1996) 331

[9] C. S. V. Stert, W. Radloffa, I. Hertel. Ultrafast photoelectron spectroscopy: Femtosecond pump-probe coincidence detection of ammonia cluster ions and electrons. *The European Physical Journal D - Atomic, Molecular, Optical and Plasma Physics* **5** (1999) 97

[10] C. Dzionk, W. Fiedler, M. v. Lucke, P. Zimmermann. Photoion Spectroscopy in the 4d Giant Resonances of the Lanthanides. *Phys. Rev. Lett.* **62** (1989) 878

[11] A. E. Boguslavskiy, J. Mikosch, A. Gijsbertsen, M. Spanner, S. Patchkovskii, N. Gador, M. J. J. Vrakking, A. Stolow. The Multielectron Ionization Dynamics Underlying Attosecond Strong-Field Spectroscopies. *Science* **335** (2012) 1336

[12] M. Bainschab. *Investigation of Multi-Photon Ionization Channels using Photo-Electron-Photo-Ion-Coincidence-Spectroscopy.* Master's thesis, TU Graz, 2016

[13] E. E. Rennie, A.-M. Boulanger, P. M. Mayer, D. M. P. Holland, D. A. Shaw, L. Cooper, L. G. Shpinkova. A Photoelectron and TPEPICO Investigation of the Acetone Radical Cation. *The Journal of Physical Chemistry A* **110** (2006) 8663

[14] J. Ullrich, R. Moshammer, A. Dorn, R. Dörner, L. P. H. Schmidt, H. Schmidt-Böcking. Recoil-ion and electron momentum spectroscopy: reaction-microscopes. *Reports on Progress in Physics* **66** (2003)

[15] R. Dörner, V. Mergel, O. Jagutzki, L. Spielberger, J. Ullrich, R. Moshammer, H. Schmidt-Böcking. Cold Target Recoil Ion Momentum Spectroscopy: a 'momentum microscope' to view atomic collision dynamics. *Phys. Rep.* **330** (2000) 95

[16] H. Enqvist. *A setup for efficient frequency tripling of high-power femtosecond laser pulses.* Master's thesis, Lund University, 2004

[17] C. Gösweiner. *Konstruktion und Charakterisierung eines Laserstrahlprofilmessgerätes.* Bachelor's thesis, TU Graz, 2012

[18] L. J. Frasinski, K. Codling, P. A. Hatherly. Covariance Mapping: A Correlation Method Applied to Multiphoton Multiple Ionization. *Science* **246** (1989) 1029

[19] V. Stert, W. Radloff, T. Freudenberg, F. Noack, I. V. Hertel, C. Jouvet, C. DedonderLardeux, D. Solgadi. Femtosecond time-resolved photoelectron spectra of ammonia molecules and clusters. *EPL (Europhysics Letters)* **40** (1997) 515

[20] N. Rusteika, K. B. Moeller, T. I. Solling. New insights on the photodynamics of acetone excited with 253-288nm femtosecond pulses. *Chemical Physics Letters* **461** (2008) 193

[21] R. Y. Brogaard, T. I. Sølling, K. B. Møller. Initial Dynamics of The Norrish Type I Reaction in Acetone: Probing Wave Packet Motion. *J. Phys. Chem. A* **115** (2011) 556

[22] Y. Haas. Photochemical α-cleavage of ketones: revisiting acetone. *Photochem. Photobiol. Sci.* **3** (2004) 6

[23] T. Shibata, T. Suzuki. Photofragment ion imaging with femtosecond laser pulses. *Chemical Physics Letters* **262** (1996) 115

[24] E. W.-G. Diau, C. Kötting, A. H. Zewail. Femtochemistry of Norrish Type-I Reactions: I. Experimental and Theoretical Studies of Acetone and Related Ketones on the S1 Surface. *ChemPhysChem* **2** (2001) 273

[25] W.-K. Chen, J.-W. Ho, P.-Y. Cheng. Isotope effects in the ultrafast photodissociation of acetone 3s Rydberg state excited at 195nm. *Chemical Physics Letters* **415** (2005) 291–295

[26] W.-K. Chen, P.-Y. Cheng. Ultrafast Photodissociation Dynamics of Acetone at 195 nm: II. Unraveling Complex Three-Body Dissociation Dynamics by Femtosecond Time-Resolved Photofragment Translational Spectroscopy. *The Journal of Physical Chemistry A* **109** (2005) 6818

[27] W.-K. Chen, J.-W. Ho, P.-Y. Cheng. Ultrafast photodissociation dynamics of the acetone 3s Rydberg state at 195 nm: a new mechanism. *Chemical Physics Letters* **380** (2003) 411

[28] Q. Zhong, L. Poth, A. W. Castleman. Ultrafast dissociation dynamics of acetone: A revisit to the S_1 state and 3s Rydberg state. *J. Chem. Phys.* **110** (1999) 192

[29] J. C. Owrutsky, A. P. Baronavski. Ultrafast photodissociation dynamics of the S1 and S2 states of acetone. *The Journal of Chemical Physics* **110** (1999) 11206

[30] J. C. Owrutsky, A. P. Baronavski. Ultrafast studies of the photodissociation of the acetone 3s Rydberg state at 195 nm: Formation and unimolecular dissociation of the acetyl radical. *The Journal of Chemical Physics* **108** (1998) 6652

[31] P. Farmanara, V. Stert, W. Radloff. Ultrafast photodissociation dynamics of acetone excited by femtosecond 155 nm laser pulses. *Chemical Physics Letters* **320** (2000) 697

[32] T. I. Solling, E. W.-G. Diau, C. Kötting, S. De Feyter, A. H. Zewail. Femtochemistry of Norrish Type I Reactions: IV. Highly Excited Ketones—Experimental. *ChemPhysChem* **3** (2002) 79

[33] M. Nobre, A. Fernandes, F. Ferreira da Silva, R. Antunes, D. Almeida, V. Kokhan, S. V. Hoffmann, N. J. Mason, S. Eden, P. Limao-Vieira. The VUV electronic spectroscopy of acetone studied by synchrotron radiation. *Phys. Chem. Chem. Phys.* **10** (2008) 550

[34] P. Sandor, A. Zhao, T. Rozgonyi, T. Weinacht. Strong field molecular ionization to multiple ionic states: direct versus indirect pathways. *Journal of Physics B: Atomic, Molecular and Optical Physics* **47** (2014) 124021

[35] P. Farmanara, W. Radloff, V. Stert, H.-H. Ritze, I. V. Hertel. Real time observation of hydrogen transfer: Femtosecond time-resolved photoelectron spectroscopy in the excited ammonia dimer. *J. Chem. Phys.* **111** (1999) 633

[36] I. Wilkinson, A. E. Boguslavskiy, J. Mikosch, J. B. Bertrand, H. J. Wörner, D. M. Villeneuve, M. Spanner, S. Patchkovskii, A. Stolow. Excited state dynamics in SO2. I. Bound state relaxation studied by time-resolved photoelectron-photoion coincidence spectroscopy. *The Journal of Chemical Physics* **140** (2014) 204301

[37] J. C. Traeger, R. G. McLoughlin, A. Nicholson. Heat of formation for acetyl cation in the gas phase. *Journal of the American Chemical Society* **104** (1982) 5318

[38] E. W. G. Diau, C. Kötting, T. I. Sølling, A. H. Zewail. Femtochemistry of Norrish Type I Reactions: III. Highly Excited Ketones—Theoretical. *ChemPhysChem* **3** (2002) 57

[39] S. Larochelle, A. Talebpour, S. L. Chin. Non-sequential multiple ionization of rare gas atoms in a Ti:Sapphire laser field. *Journal of Physics B: Atomic, Molecular and Optical Physics* **31** (1998) 1201

Danksagung

Der sicherlich größte Dank gebührt meinem Betreuer Ass.Prof. Dr. Markus Koch, dessen tatkräftige Unterstützung in fachlichen Fragen und bei praktischen Problemen im Labor, sowie das persönliche Betreuungsverhältnis maßgeblichen und entscheidenden Anteil am Erfolg der Arbeit haben. Die hohe Bereitschaft Wissen und Fertigkeiten weiterzugeben, sein großer persönlicher Einsatz und die Begeisterung an der Sache waren und sind Vorbild und Ansporn zugleich.

Herrn Univ.-Prof. Dr. Wolfgang E. Ernst gilt mein Dank für die Möglichkeit am Institut für Experimentalphysik an aktueller Forschung mitwirken zu können. Die hochmodernen experimentellen Möglichleiten am Institut sowie die fachliche Breite und Tiefe der Institutsmitglieder stellen einen idealen Nährboden für wissenschaftliches Arbeiten dar.

Meinem Laborpartner Markus Bainschab möchte ich für die gute und harmonische Zusammenarbeit danken. Erst die Arbeit im Team ermöglichte das Bedienen und Weiterentwickeln des komplexen experimentellen Setups. Die Diskussion und das gemeinsame Überwinden auftretender Hindernisse machten die Monate im Labor zu einer produktiven und auch unterhaltsamen Zeit.

Pascal Heim und Bernhard Thaler gilt mein Dank für die gute Zusammenarbeit und die gegenseitige Unterstützung innerhalb der Arbeitsgruppe.

Weiters möchte ich mich bei meinen Studienkollegen bedanken, mit denen gemeinsam ich unzählige Stunden in Vorlesungen und Laboren, mit Rechenübungen und verschiedensten physikalischen und nicht-physikalischen Fragestellungen verbringen durfte. Nicht zuletzt die stets gute Gemeinschaft und der Zusammenhalt haben mein Studium stark geprägt. Neben Markus Bainschab möchte ich an dieser Stelle Ralf Meyer, sowie Christian Platzer, Michael Rumetshofer, Alexander Schiffmann, Michael Draxler und Alexander Schossmann nennen.

Auch meinem Mitbewohner David Großschädl gilt mein Dank. Das unkomplizierte Zusammenleben, sowie die vielen Diskussionen, waren wichtiger Bestandteil meiner Studienzeit.

Mein Studienabschluss besteht nicht alleine aus meiner eigenen Leistung sondern ist auch das Resultat großer und bedingungsloser Unterstützung seitens meiner Familie. Meine Eltern Veronika und Franz, meine Großeltern, sowie mein Bruder Florian waren stets unverzichtbare Stützen und haben mir mein Studium erst ermöglicht.